MAK: Reconstructing cosmic history

Jarno Ruwen
Supervisor: Prof. dr. R. van de Weygaert

September 19, 2011

Contents

Chapter 1

Introduction

When we look around us, we see a lot of *structure*, on many different scales. Looking down, we see the Earth. Looking up at the sky we see the Sun, or at night the Moon, planets and stars. On a much larger scale, we can see the light of the Milky Way galaxy stretched across a dark sky. You may also see our neighbour, the Andromeda galaxy. On the southern hemisphere, you see our companion galaxies the Magellanic clouds. Using our astronomical instruments, we can see structures on even larger scales. For example, one can clearly see clusters of galaxies with a telescope, and sometimes even the filaments that connect them. For a better view of structure on large scales, we need to measure distances in order to build a three-dimensional picture. Thus we can not only see clusters and filaments, but also void regions without any galaxies. These would not be visible without the distance measurement, because structures in the fore- and background intersect with them. A slice through such a three-dimensional map of galaxies is shown is Figure 1.1.

The discovery of the cosmic microwave background (CMB) radiation, and its subsequent mapping by experiments like COBE and WMAP (Bennett et al., 1996; Komatsu et al., 2011), has confirmed the Big Bang theory, which states that the universe started out as very small and dense point that expanded rapidly and cooled down in the process. We also learned that our universe started out extremely homogeneous: the structures seen today were seeded in tiny perturbations (in the order of $\sim 10^{-5}$) in the early universe. The slight overdensities started to collapse under their own gravity and formed the large scale structure mentioned above. In addition, they seeded many smaller structures like galaxies, stars and planets.

We know that the matter distribution went from nearly homogeneous to the structure we see today, but how this process of evolution works exactly is still under study. Many of these studies construct a theoretical model of the physics that dominates structure formation on large scales, and test this model in computer simulations. If the structures in the simulation results look like the structures we observe, the model is a good approximation of reality. Models that are based on the Lagrangian perturbation theory, like the linear Zel'dovich approximation and the more advanced Adhesion model (Zel'Dovich, 1970; Sahni et al., 1994), already give a good approximation of the evolution of the large scale structure. In these models the initial perturbations are transformed into peculiar velocities for the particles at

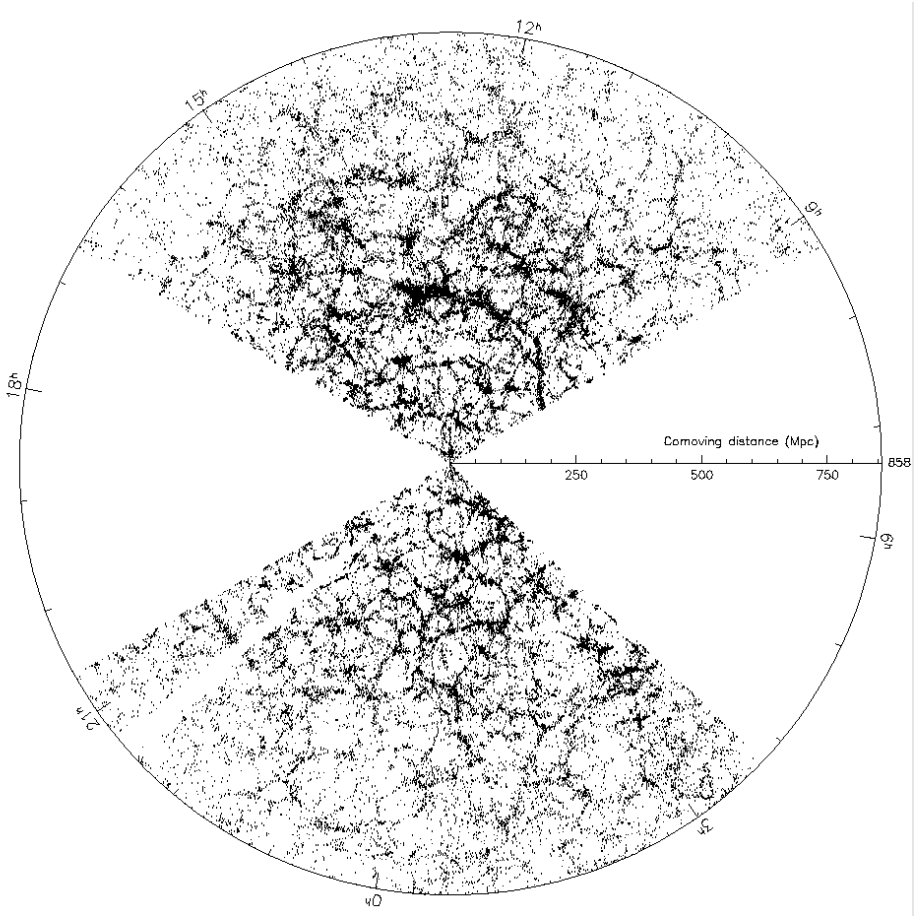

Figure 1.1: **The large scale structure of the universe.** The Sloan Digital Sky Survey obtained distances for thousands of galaxies. A clear structure of clusters, filaments and voids is visible in the distribution of galaxies. Figure by SDSS-III collaboration (2011).

the start of the simulation. The structure then forms, because the particles move towards certain regions and away from others. The trajectories of the particles will inevitably cross in high density regions, causing unphysical behaviour. How the model deals with this trajectory crossing is of great influence on the accuracy of the model.

These models give a very good approximation of the universe before high density structures form. However, once they have formed, the evolution of structure becomes highly non-linear and the approximation breaks down. In the non-linear regime you will need a model that incorporates gravitational forces in a non-linear way. These are commonly called N-body simulations. They simulate the physical processes of structure formation: all particles exert a gravitational force on each other and this drives the structure formation in these simulations, just like in reality. This allows the models to remain accurate in the non-linear regime. Most modern simulations also include gas pressure, which is important to accurately simulate the formation of high density regions. N-body simulations are subject to a certain cosmology, which determines the properties of the universe's spacetime. An import cosmological ingredient is dark energy. This is an unknown form of energy responsible for an accelerating

expansion of spacetime. Observations suggest that our universe has such an energy component (Riess et al., 1998, e.g.), on which we will elaborate in Chapter 2. Since we are not yet able to determine what the origin of this dark energy is, it is an import subject in the latest studies with N-body simulations.

Recent works have shown that the specific implementations of dark energy models can have a mild influence on the development of structures. This is reflected in various observables like the (large scale structure) power spectrum (Baldi, 2011), the halo mass function (de Boni et al., 2011) and the shapes of voids (Lee and Park, 2009; Lavaux and Wandelt, 2010). The focus of our project is on the latter of these three. Voids originate in Gaussian random fluctuations, which are approximately spherical. As the cosmic structures evolve, the voids will deviate from this sphericity. It appears that in certain models, where the growth rate of structures is high, the voids get more ellipsoidal shapes after a certain time. We hope to confirm this finding for five dark energy models of our own. A more extensive background for this will be provided in Chapter 4.

The basis of our analysis of void shapes will be the Lagrangian formalism. This is quite different from the common Eulerian framework, where the contents of the universe are studied in a fixed coordinate frame. In the Lagrangian formalism the properties are not described for certain coordinates, but for a certain test volume of matter which can move around, expand or collapse and change in shape. The deformation of a volume in the Lagrangian analysis reflects the shape of a structure in the Eulerian framework. A more detailed description of the Lagrangian formalism is given in Chapter 3.

A technique called the Monge-Ampère-Kantorovitch reconstruction (MAK) allows us to obtain the necessary information for the Lagrangian analysis. This technique attempts to reconstruct where the matter originated that now forms the large scale structure. Simply put, the MAK reconstruction tries to transport an initial uniform field of particles to a given set of particle positions (these can be from dark matter or from galaxies) in such a way that the minimal amount of energy is used in the transportation. Since nature always tries to find the path of lowest energy, this reconstruction is a good approximation of where the matter in a structure actually originated. The reconstructed displacements of mass are an approximation of the peculiar velocity as well, providing dynamical information that cannot be observed. Chapter 3 describes this reconstruction technique in detail and provides the algorithm used for it.

The information obtained from this reconstruction can be used in the Lagrangian analysis. The deformation of a volume can be calculated from the displacements of mass. In our case it is used to calculate the ellipticity of a void. When this method is applied to a few time steps from an N-body simulation, it allows us to study the evolution of the void shapes. This is done for different dark energy models to study the influence of dark energy on void ellipticity. Since we have access to the dark matter distribution in these simulations as well as the positions of haloes (clumps of dark matter, which are the seeds for galaxies) we can also check if dark matter and galaxies follow the same trends. Whether these models show a significant difference in their influence on void shapes can be read in Chapters 5 and 6.

Chapter 2

The Universe

In this chapter we will elaborate on the contents of the universe and on the physics of its evolution. We will start with the birth of the universe, the Big Bang. In the next sections we will look at the dark side of our universe. Dark matter and dark energy play an important role in structure formation, so we will shortly introduce those concepts. In Section 2.3 of this chapter we will explain cosmology, the physics of the universe as a whole. This section will also explain how dark matter and dark energy can influence the cosmology.

2.1 The Big Bang

The large scale structure is thought to originate from only moments after the Big Bang, i.e. the birth of the universe, from the epoch of inflation. During this epoch, the universe expanded by a factor of at least $\sim 10^{60}$ in a very short time ($\sim 10^{-33}$ s; Lyth and Riotto, 1999). The tiny energy fluctuations that were present before inflation, expanded along with the universe. As a result the fluctuations got 'frozen' and were imprinted in the dark matter. After inflation, but still within the first second of its existence, the contents of the universe went through various phases with different states of energy and matter. While it was expanding even further, the contents of the universe cooled down, and various particles like quarks and electrons were created. These subsequently clumped together to form protons and neutrons. After a few minutes, nuclei like deuterium and helium were formed as well. The universe then contained a plasma of photons, nuclei and electrons. The free electrons are coupled to the photons because they are very effective at scattering photons. Because of this coupling, the high pressure of the photon fluid is shared with the baryons. As a result, the gravitational collapse of high density fluctuations is prevented by the pressure build-up in the photons. These counteracting effects cause harmonic oscillations in the plasma fluid. Resonances in these oscillations occurred on certain scales, which determined the scales at which structures were formed later. When the plasma cooled down to the point where the photons could not ionize a recombined proton-electron pair anymore, the photons decoupled from the matter and all nuclei and electrons were combined to form atoms. The decoupled photons were then, for the lack of free electrons, free to travel to Earth where we could observe them as the CMB. The perturbations in the density of the matter are visible as temperature anisotropies, (see Figure 2.1).

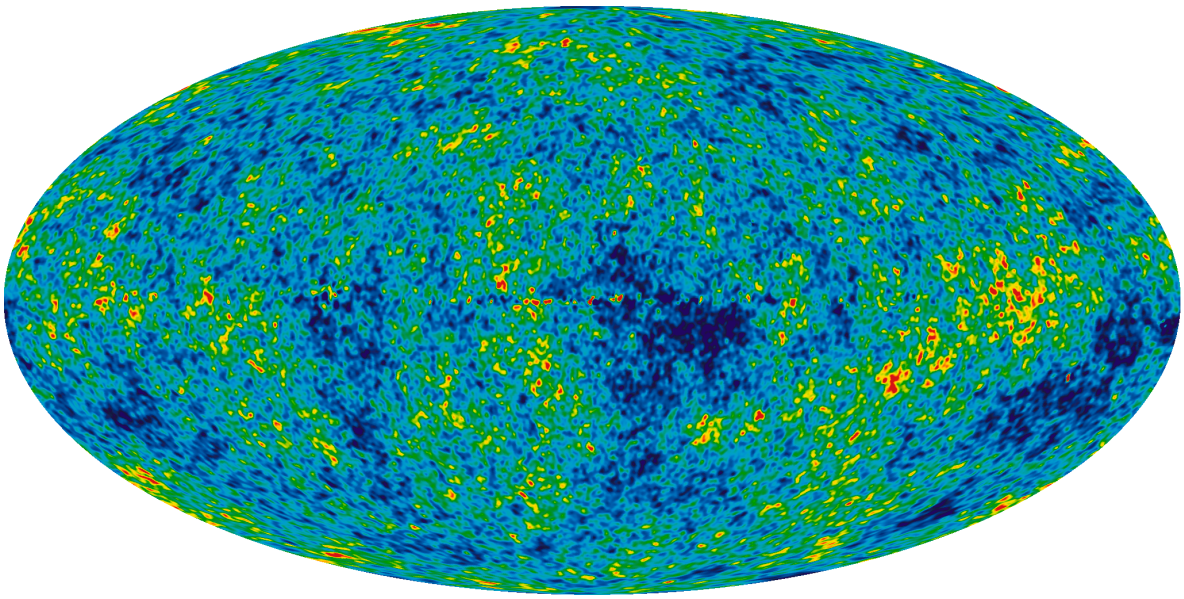

Figure 2.1: **The cosmic microwave background** as imaged by the WMAP satellite. The fluctuations visible in this map are the seeds for the large scale structure. Figure from Komatsu et al. (2011).

2.2 Dark matter

Starting with early observations of the dynamics of galaxy pairs, groups and clusters, questions had been raised whether we can see all mass present in galaxies (Zwicky, 1937). This question came back into focus when evidence for missing mass came from the observation of the rotation speed of galaxies. In the 1970s stronger proof was presented that there was indeed more mass than we could see. Using the light distribution and an estimated mass-to-light ratio, a prediction for the shape of the rotation curve was made. This curve shows a peak in the bulge region and has a Keplerian decline in the disc region ($v \propto r^{-\frac{1}{2}}$). It was compared to the velocity curve of a galaxy, constructed from the observed Doppler shift of the 21-cm line of neutral hydrogen gas. This curve showed the same peak in the bulge region, but there was hardly any decline in the disk region (see Figure 2.2 for sketches of both curves). Given that the mass-to-light ratio is approximately constant throughout the disk, this means that the mass density in the disk remains significantly high all the way to the edge where hardly any matter can be observed. Because this is a significant amount of mass that does not seem to emit any radiation, it was called '*dark matter*'. An extensive review of early observations and discoveries related to the missing mass in rotation curves is given by Faber and Gallagher (1979).

From this time on many candidates for dark matter have been proposed, ranging from omni-present tiny particles like neutrinos to elusive compact objects like MACHO's or black holes. Many of these candidates have been rejected, and none have been verified as the species we are actually looking for. But for our purposes it is irrelevant what this dark matter exactly is. It is only important that the dark matter candidate interacts with the rest of the universe exclusively through the gravitational force and that the electromagnetic interaction is very

weak or non-existent.

Dark matter is an important aspect in the development of the large scale structure displayed in Figure 2.3. It is the driving force behind the gravitational collapse of the seeds for these structures. Radiation or gas pressure can prevent the collapse of baryonic matter. Dark matter only interacts with other particles through gravity, so it does not feel pressure. Therefore it will always cause density perturbations to grow and form structures. This was particularly true in the early universe before recombination. Radiation has a high pressure, thus it tends to smooth its (energy) distribution, much like gas does on small scales. Because the baryonic matter was tightly coupled to the radiation before recombination, its mass distribution was also smoothed out. This effect can be quantified by the Jeans mass. The Jeans instability theorem describes the balance between the inward gravitational force and outward pressure in a baryonic gas. From the balance of these force one can derive a characteristic mass, the Jeans mass. Structures with a mass lower than the Jeans mass can not collapse because the pressure is greater than the gravity. Only structures above the Jeans mass have enough gravity to overcome the pressure and collapse. Before recombination the Jeans mass was very high for baryonic matter ($M_J > 10^{15} M_\odot$; Ryden, 2003), because of the high radiation pressure. Therefore, baryons did not grow structures below this limit. Dark matter on the other hand was not coupled to the radiation as it does not interact through electromagnetic forces. Hence it effectively has a Jeans mass of zero, and grows structures on all scales.

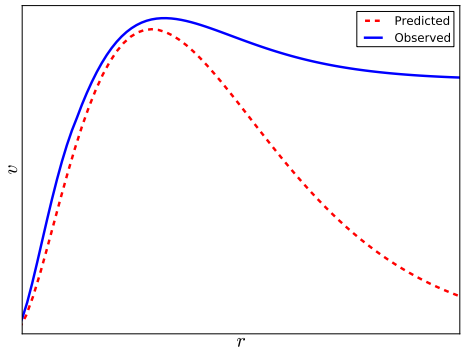

Figure 2.2: **A sketch of the rotation curve for a spiral galaxy.** The dashed curve shows what was expected on the basis of the light distribution. The solid curve shows the trend that was actually measured.

After recombination the radiation pressure does not affect the baryons anymore and the Jeans mass drops dramatically to a value of $M_J \sim 10^6 M_\odot$ (approximately the mass of a large globular cluster or small dwarf galaxy). The baryonic matter is now also free to collapse down to these scales. Because dark matter has already been growing structures on all scales, the baryons will simply be pulled towards the overdensities in the dark matter. Baryons and dark matter now have the same behaviour, so the main effect of dark matter is a faster collapse of structures than would have been the case with just baryonic matter. Approximately 80% of all matter is dark, so structures collapse much faster than they would have without it. Because there is so much dark matter, it also influences the evolution of the universe as a whole. As gravity is the only force exerted by dark matter, it tends to accelerate the collapse of the universe. In practice, this means it just slows down the expansion. The evolution of the universe, and the dark matter's role therein, will be explained in the next section.

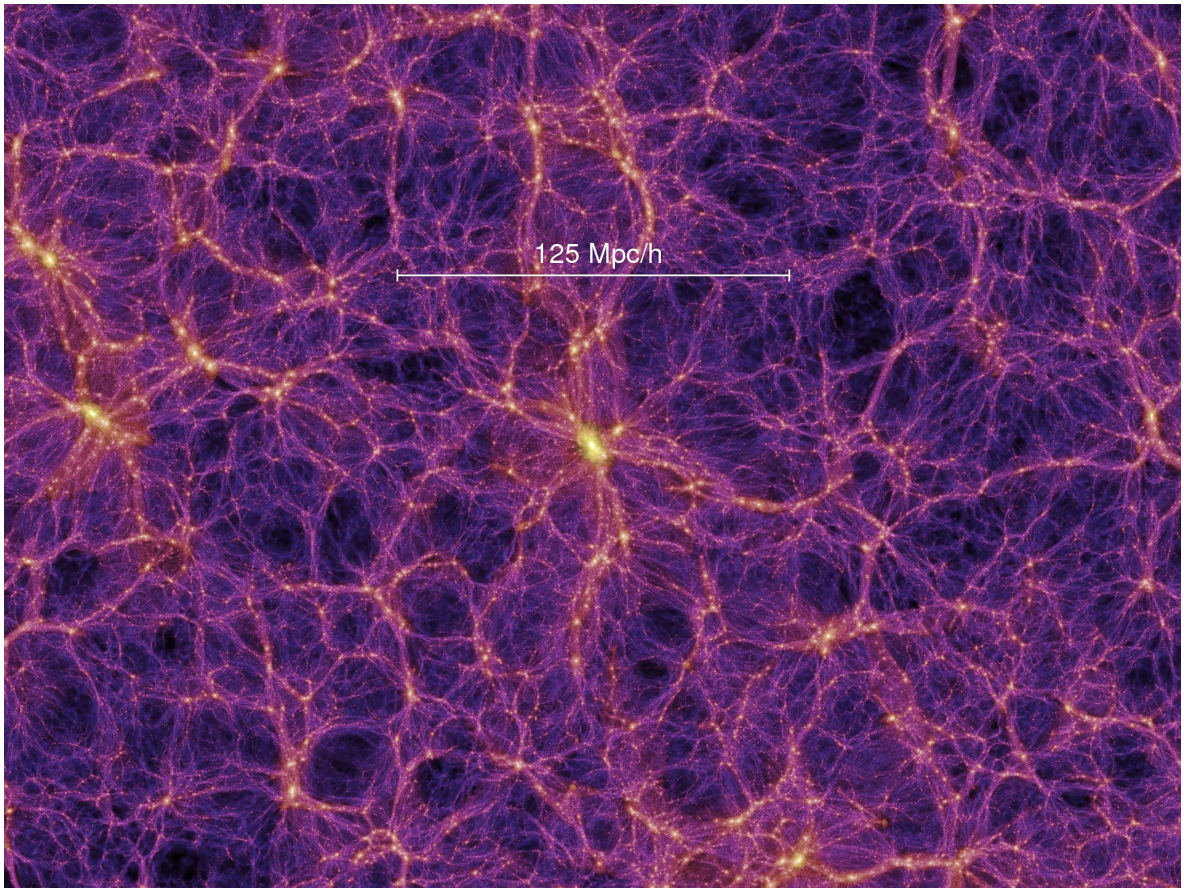

Figure 2.3: **The Millennium simulation: one of the largest N-body simulation to date.** This is a 15 Mpc thick slice from the simulation, centered on the largest cluster in the simulation. The colours represent the dark matter density. Image courtesy of VIRGO Consortium.

2.3 Friedman-Robertson-Walker-Lemaître models

When we compare the universe we see around us today to what it looked like at the epoch of recombination, we see that big changes have occurred. The universe went from a nearly uniform gas to structures with high over- and underdensities on all scales. To study this transition, we need to know some properties of the universe. The collapse of structures is not only an effect of gravity, but it is also influenced by properties of space like (global) curvature and expansion rate. We begin with a few assumptions. Most important is the cosmological principle: the notion that the universe is isotropic (the same in all directions) and homogeneous (the same everywhere). This is certainly not valid on small scales, but it does seem to hold on scales $> 300\,\mathrm{Mpc}$. This assumption implies that we live in a three-dimensional space that is flat (no curvature), spherical (positive curvature) or hyperbolic (negative curvature). These properties can be described by a metric for spacetime. A metric expresses how a distance in a spacetime depends on displacements in each coordinate. The metric that meets our criteria is called the Friedman-Robertson-Walker-Lemaître metric (Walker, 1937,

and reference therein):

$$ds^2 = dt^2 - a^2(t)\left[dr^2 + R_c^2 S_k(\tfrac{r}{R_c})^2\left(d\theta^2 + \sin^2\theta d\phi^2\right)\right]. \tag{2.3.1}$$

This expression contains the size of a line element ds, the coordinates (t, r, θ and ϕ), the scale factor $a(t)$ (a measure for the expansion of space) and the curvature function $S_k(\frac{r}{R_c})$. This curvature function represents the Gaussian curvature of space and the associated changes of the metric. When the universe has flat space the curvature index is $k = 0$ and $S_0(\frac{r}{R_c}) = r$. For positively and negatively curved space the indices are $k = +1$ or $k = -1$ respectively. The corresponding function for positive curvature is $S_{+1}(\frac{r}{R_c}) = r\sin(r/R_c)$, and for negative curvature $S_{-1}(\frac{r}{R_c}) = r\sinh(r/R_c)$. Observational evidence from the WMAP mission is currently consistent with flat space. Curved space is still possible, but only with a large radius of curvature R_c (Komatsu et al., 2011).

The scale factor is a measure for the expansion of the universe: $a(t) = R(t)/R_c$. Usually it is normalized to $a(t_0) = 1$ at present time. The value (and evolution) of $a(t)$ is not specified. Einstein's field equations of general relativity have to be used to specify $a(t)$. With the above metric, the analytic solution to these field equations are the Friedman equations:

$$H^2 = \left(\frac{\dot{a}}{a}\right)^2 = \frac{8\pi G}{3}\rho - \frac{kc^2}{R_c^2 a^2} + \frac{\Lambda c^2}{3}, \tag{2.3.2}$$

$$\left(\frac{\ddot{a}}{a}\right) = -\frac{4\pi G}{3}\left(\rho + \frac{3p}{c^2}\right) + \frac{\Lambda c^2}{3}. \tag{2.3.3}$$

The first equation is for the expansion rate of the universe, described by the Hubble parameter $H(t)$. It depends on the energy density ρ, the curvature parameter k and on the cosmological constant Λ. Einstein added this constant to his field equations to create a static universe. Although the notion that the universe is static has long since been rejected, Λ is now used as a form of dark energy to explain the accelerating expansion of the universe. This dark energy will be explained in the next section.

The second equation is for the acceleration of the expansion rate. It also depends on ρ and Λ and on the pressure p. The left hand side is sometimes replaced by the deceleration parameter

$$q = -\frac{\ddot{a}a}{\dot{a}^2} = -H^{-2}\frac{\ddot{a}}{a}$$

for historical reasons. To be able to solve these equations we need to know the relation between the pressure and the density, which is given by the equation of state. The pressure term can then be replaced by an additional density term using this relation. Each component of the universe has its own equation of state. Baryonic and dark matter are usually assumed to be pressureless dust ($p = 0$) and radiation has $p = \frac{1}{3}\rho c^2$.

The energy contribution of the different components of the universe is usually written in terms of the critical density ρ_c. The critical density is the density of a flat, matter dominated universe for a given Hubble parameter:

$$\rho_c(t) = \frac{3H(t)^2}{8\pi G}. \tag{2.3.4}$$

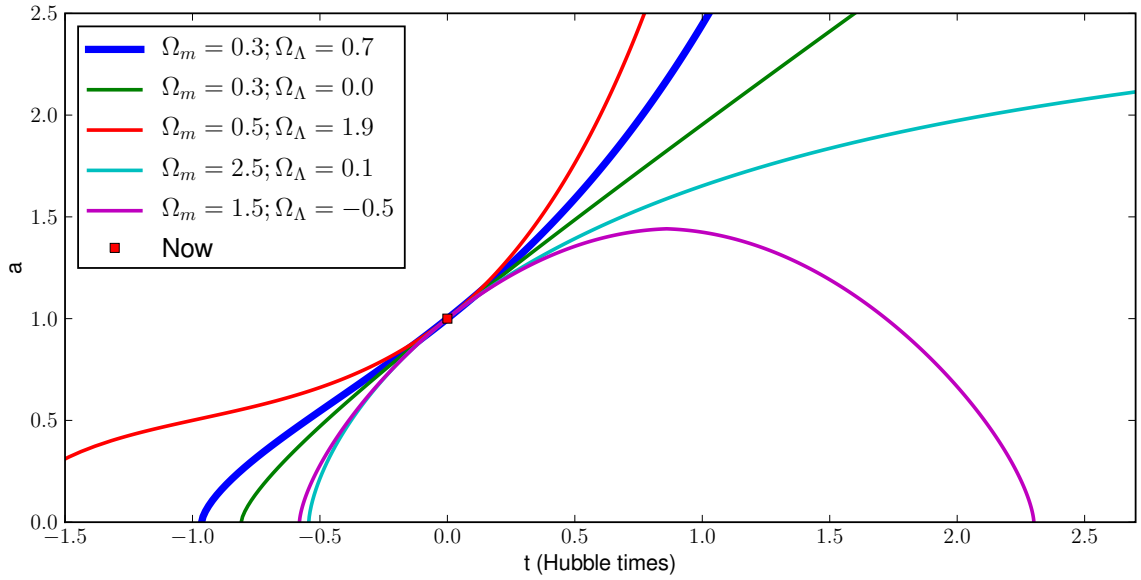

Figure 2.4: **The evolution of universes** with different contents, as measured by the scale factor $a(t)$. The thick blue line is an approximation of our own universe. It is evident that the age and the final destiny of a universe depend on the amount of matter and dark energy. All universes are normalized to have the same scale factor and Hubble constant at present time.

We can now define a matter density parameter that gives the density as a fraction of the critical density:

$$\Omega_m(t) = \frac{\rho_m(t)}{\rho_c(t)} = \frac{8\pi G}{3H^2}\rho_m(t). \tag{2.3.5}$$

In analogy to this we can construct density parameters for the other components of the universe as well:

$$\Omega_r(t) = \frac{8\pi G}{3H(t)^2}\rho_r \tag{2.3.6}$$

$$\Omega_\Lambda(t) = \frac{c^2}{3H(t)^2}\Lambda \tag{2.3.7}$$

$$\Omega_k(t) = -\frac{c^2}{H(t)^2 R_c^2 a(t)^2}k \tag{2.3.8}$$

Here, Ω_r is the density parameter for radiation. Radiation did not appear in the previous formulas because it was contained in the full energy density. We now introduce it as a separate component because it evolves differently from (dark) matter.

We can now rewrite the first Friedman Equation (Eq. 2.3.2) in terms of the current values of these density parameters (e.g. $\Omega_{m,0} = \rho_{m,0}/\rho_{c,0}$). This gives a better understanding of how each component evolves. The energy density has been split into the separate contributions from radiation and (dark) matter,

$$H^2 = H_0^2\left(\Omega_{r,0}a^{-4} + \Omega_{m,0}a^{-3} + \Omega_{k,0}a^{-2} + \Omega_{\Lambda,0}\right). \tag{2.3.9}$$

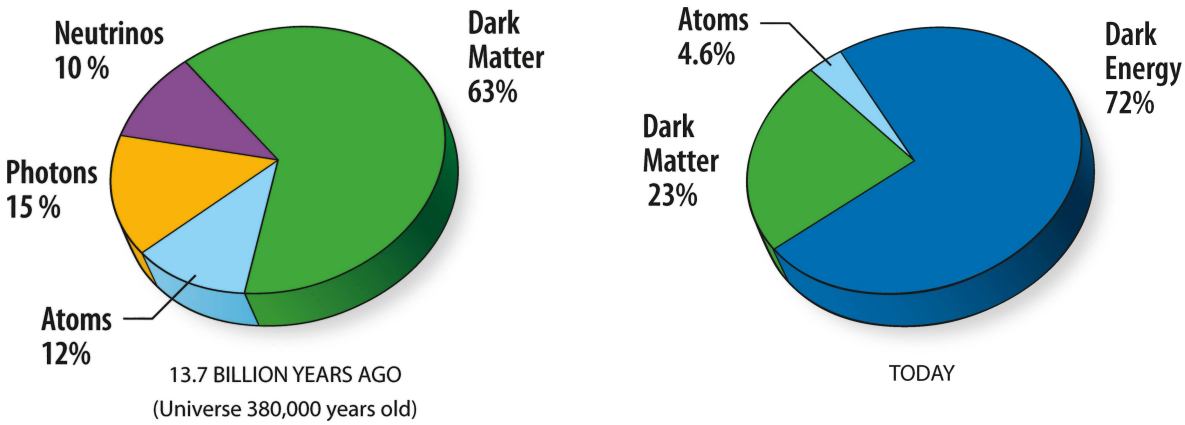

Figure 2.5: **The contents of the universe now and before recombination.** Picture from NASA.

$\Omega_{m,0}$ evolves as $a(t)^{-3}$ because the matter density decreases proportional to the increase in volume. The radiation energy density falls even faster with time than the matter density. In addition to the dilution by the stretching of space, each photon also loses energy as its wavelength increases proportional to $a(t)$. The contribution from radiation was important in the early universe, but since then it has reduced to an insignificant $\Omega_{r,0} \sim 10^{-5}$ (see Figure 2.5). The energy density of the cosmological constant Λ does not change with time. This also means that Λ is insignificant in the early universe, because the densities of the other components are much higher for small values of $a(t)$. An important aspect of observational cosmology is the determination of these constants. The most recent constraints from WMAP data (Komatsu et al., 2011) combined with supernova and Cepheid observations (Hicken et al., 2009; Riess et al., 2009) are (see Figure 2.5):

$$\Omega_{b,0} = 0.0458 \pm 0.0016 \tag{2.3.10}$$
$$\Omega_{DM,0} = 0.229 \pm 0.015 \tag{2.3.11}$$
$$\Omega_{\Lambda,0} = 0.725 \pm 0.016 \tag{2.3.12}$$
$$H_0 = 70.2 \pm 1.4\, km\, s^{-1}\, Mpc^{-1} \tag{2.3.13}$$

The values listed above are determined for a flat universe ($\Omega_k = 0$). The errors are much larger if Ω_k is not fixed. Komatsu et al. (2011) also determined some constraints on how flat the universe actually is by inspecting the angular size of the largest fluctuation in the CMB. A value of $\sim 1^o$ would correspond to a flat universe. A larger diameter means there is a positive curvature and a smaller means a negative curvature. In a standard cosmological model the curvature is within $-0.0178 < \Omega_{k,0} < 0.0063$. These values are slightly different from the ones used in this project, since the dark energy models for the simulations were based on WMAP data release 3 (those values are listed in Chapter 6).

2.4 Dark energy

In the previous section a new component of the universe was introduced in the Friedman equations: dark energy. It was introduced in the form of a cosmological constant Λ for its

simplicity, but dark energy may be more complicated. The general defining property of dark energy is a negative pressure. This implicates that, as a volume expands it will contain more dark energy. The cosmological constant from the previous section has a constant energy density such that the increase in energy content is always proportional to the increase in volume of the expanding space. In this section the more general concept of dark energy will be discussed and the evidence for its presence will be presented.

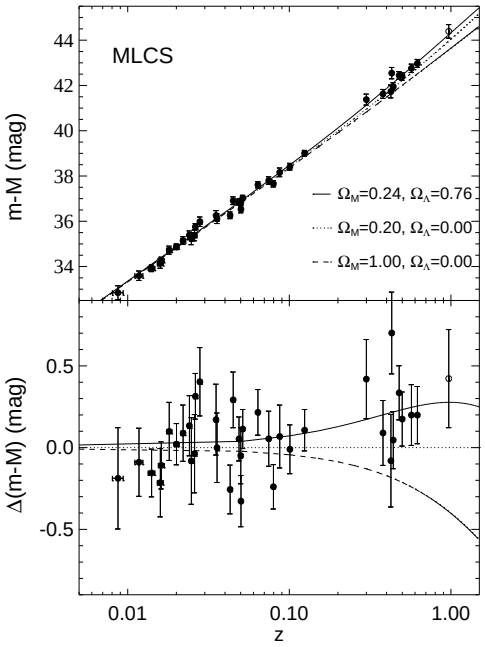

Figure 2.6: **Hubble diagram for supernovae type Ia.** A Hubble diagram shows the distance as a function of redshift. For the supernovae the distance modulus is used to obtain a distance from the measured magnitude. For comparison the function for three cosmologies is also plotted. In the bottom panel the same data is displayed, but normalized to the curve of the matter dominated universe with $\Omega_m = 0.2$. It is clear that the universe with a dark energy component is the better fit. Figure from Riess et al. (1998).

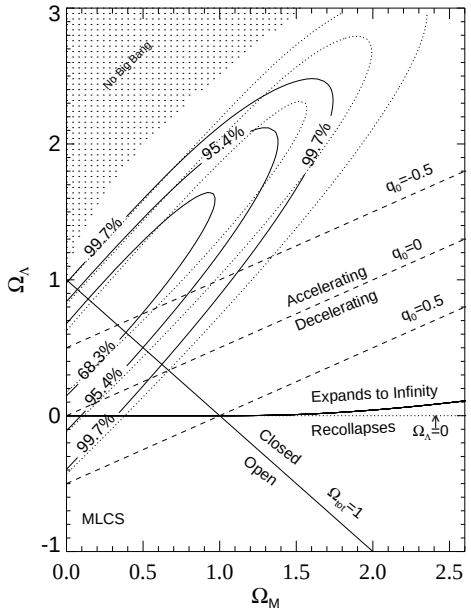

Figure 2.7: **The constraints on Ω_m and Ω_Λ from observations of supernovae.** The ellipses show the confidence intervals from supernova data. If the universe has negligible curvature ($\Omega_{tot} = 1$), this diagram shows that the most likely values for the contents of the universe are close to $\Omega_m = 0.3$ and $\Omega_\Lambda = 0.7$. Figure from Riess et al. (1998).

There are many different models for dark energy, but by definition it needs to have *negative pressure*. This is necessary to explain the accelerating expansion of the universe. The relation between the amount of dark energy and the pressure it exerts is governed by the equation of state (EoS). For the cosmological constant it reads $P_\Lambda = -\rho_\Lambda$. Other models do not have a fixed relation between the density and pressure. The EoS of such models is written is $P = w(a)\rho c^2$, where $w(a)$ depends on the scale factor $a(t)$, but is somewhere in the range $-1 \leq w \leq -\frac{1}{3}$.

Evidence for dark energy can be found in many different ways. Among them are the evolution of the galaxy cluster mass function (Vikhlinin et al., 2009), the power spectrum of the CMB (Komatsu et al., 2011) and the evolution of void shapes (Lee and Park, 2009). The most compelling evidence, however, is from detailed observations of the redshifts of supernovae type Ia (Riess et al., 1998). Supernovae of type Ia can be used as standard candles, because they always have nearly the same absolute magnitude. For this reason it is possible to determine the distance to these faraway objects independent of their redshift, by only using the apparent magnitude and the distance modulus. The relation between the distance and the redshift is linear in a universe expanding at a fixed rate $H(t) = H_0$, which is often used to determine distances to faraway objects. However, Riess et al. (1998) found that the supernovae at a given redshift were fainter and thus further away than would be expected from that redshift (see Figure 2.6). This means that the expansion rate at the time when these supernovae exploded was lower than the expansion rate is nowadays. In other words, the expansion of the universe seems to be accelerating.

This acceleration provides some constraints on dark energy, but it cannot by itself proof how much there is. This becomes clear when the equation for the deceleration parameter, a form of the second Friedman Equation (Eq. 2.3.3), is written in terms of the density parameters for pressureless matter ($p = 0$) and dark energy,

$$q = -\left(\frac{\ddot{a}a}{\dot{a}^2}\right) = \frac{4\pi G}{3H^2}\left(\rho + \frac{3p}{c^2}\right) - \frac{\Lambda c^2}{3H^2} = \frac{\Omega_m}{2} - \Omega_\Lambda. \tag{2.4.1}$$

The observed acceleration of expansion not only depends on dark energy, but also on the amount of matter in the universe (some examples are provided in Figure 2.6). The constaints on the amount of matter and dark energy can then be displayed by probability curves in an $\Omega_m - \Omega_\Lambda$ diagram (see Figure 2.7). The CMB provides additional information to solve this ambiguity. The curvature of space is related to the other components through $\Omega_k = 1 - \Omega_{total} = 1 - \Omega_m - \Omega_\Lambda$. Since the WMAP mission has constraint the curvature to $-0.0178 < \Omega_{k,0} < 0.0063$ (Komatsu et al., 2011, and references therein), the intersection of the line $\Omega_{total} = 1$ with the high probability region in Figure 2.7 provides a good estimate of the values for Ω_m and Ω_Λ.

2.5 Dark energy models

In Section 2.4 we have already had a short introduction into dark energy. That section focused on a cosmological contant Λ as the simplest form of dark energy. Although Λ provides an excellent explanation for the observed effects, there are some problems in setting up a physical theory that provides a cosmological constant. In this section we will look at dark energy in a broader sense and we will treat some more advanced models with a physical basis.

The basis for a dark energy model lies in the equation of state. In its simplest form, which we know as the cosmological constant, the equation of state is $P = w_0 \rho c^2$ where w_0 is a constant usually between -1 and $-\frac{1}{3}$. If we want to do something a bit more advanced we can

make a parametrisation where we split w into a constant and a linearly evolving component.

$$P = [w_0 + (1-a)w_a]\,\rho c^2 \tag{2.5.1}$$

Here w_0 is the present ($a = 1$) value for w, and w_a determines how fast it varies with time. The most common values for these constants are $w_0 \approx -1$ and $-1 < w_a < 1$. WMAP has constrained these parameters to $w_0 = 0.93 \pm 0.13$ and $w_a = 0.41 \pm 0.72$ (Komatsu et al., 2011). These methods are mostly used to study the influence of evolving dark energy on structure formation in the universe. They do not necessarily have an underlying physical theory. Of course there also are models that are based on physical theories, where the equation of state is constructed from the known behaviour of some component that offers an explanation for the accelerated expansion. The most popular example of this is the class of dark energy models based on quintessence that will be used in this project.

2.5.1 Quintessence

Quintessence, Latin for 'fifth element', is a theoretical form of energy that is a candidate for dark energy. The basic concept of the theory is a scalar field ϕ that is subject to a potential $V(\phi)$. The form of the potential can vary from model to model within the quintessence theory. In a related class of models, the scalar field is coupled to gravity. These models are based on scalar-tensor theory, and are called 'extended quintessence' models (EQ).

In a basic quintessence universe we still have the Friedman equation:

$$H^2 = H_0^2(\Omega_r + \Omega_m + \Omega_k + \Omega_\phi), \tag{2.5.2}$$

However, in this case the dark energy term Ω_ϕ depends on a variable energy density:

$$\Omega_\phi = \frac{8\pi G}{3H_0^2}\rho_\phi. \tag{2.5.3}$$

The energy density of the scalar field ρ_ϕ satisfies the continuity equation:

$$\frac{d\rho_\phi}{dt} + 3H\left(\rho_\phi + \frac{P_\phi}{c^2}\right) = 0, \tag{2.5.4}$$

which has the solution:

$$\rho_\phi = \rho_{\phi,0}\exp\left(-3\int_{a_0}^{a}\frac{1+w(a')}{a'}da'\right), \tag{2.5.5}$$

where $w(a')$ is the time dependent equation of state parameter $w = \rho_\phi c^2/P_\phi$. The density and pressure depend on the scalar field ϕ and on the potential it resides in:

$$\rho_\phi = \tfrac{1}{2}\dot{\phi}^2 + V(\phi), \tag{2.5.6}$$

$$P_\phi = \tfrac{1}{2}\dot{\phi}^2 - V(\phi). \tag{2.5.7}$$

The Klein-Gordon equation for the evolution of this scalar field is given by de Boni et al. (2011) as

$$\ddot{\phi} + 3H\dot{\phi} + \frac{\partial V(\phi)}{\partial \phi} = 0. \tag{2.5.8}$$

We can now define a specific model by choosing a potential. Brax and Martin (1999) suggested a potential based on supergravity (SUGRA for short):

$$V(\phi) = \frac{M^{4+\alpha}}{\phi^{\alpha}} e^{4\pi G\phi^2}. \tag{2.5.9}$$

Both M and $a \geq 0$ are free parameters. A similar potential was already suggested a decade earlier by Peebles and Ratra (1988):

$$V(\phi) = \frac{M^{4+\alpha}}{\phi^{\alpha}}. \tag{2.5.10}$$

A model with this potential is named after its inventors: the RP-model.

2.5.2 Extended Quintessence

In scalar-tensor theory we also have a scalar field ϕ and it is again subject to a potential $V(\phi)$, but now the scalar field is coupled to gravity (a tensor field) as well. Such theories are often defined by a Lagrangian. For this system it is:

$$\mathcal{L} = \frac{1}{2}F(\phi)R - \frac{1}{2}\partial^{\mu}\phi\partial_{\mu}\phi - V(\phi) + \mathcal{L}_{fluid}. \tag{2.5.11}$$

The first term, $\frac{1}{2}F(\phi)R$, is the coupling term between the scalar field and gravity and curvature in the form of the Ricci scalar R. The second is a kinetic term, $\frac{1}{2}\partial^{\mu}\phi\partial_{\mu}\phi$, just like the ϕ^2 we encountered in the other quintessence models. $V(\phi)$ is the potential of the scalar field and $\mathcal{L}_{fluid}$ is the classical Lagrangian of all other components that do not depend on ϕ. The coupling function is defined as:

$$F(\phi) \equiv \frac{1}{\kappa_*} + \xi(\phi^2 - \phi_0^2). \tag{2.5.12}$$

The constant $\kappa_* = 8\pi G_*$ is a modification of the Newtonian gravitational parameter $\kappa = 8\pi G$, reflecting the modified gravity. As a result of general relativity, this locally reduces to:

$$\frac{1}{\kappa_*} + \xi\phi_0^2 = \frac{1}{\kappa}. \tag{2.5.13}$$

The coupling constant can be either positive or negative, indicated as EQp or EQn respectively.

In the EQ models of de Boni et al. (2011) the energy density and pressure of the scalar field are:

$$\rho_{\phi} = \frac{1}{2}\dot{\phi}^2 + V(\phi) - 3H\dot{F}(\phi) + 3H^2\left[\frac{1}{\kappa_*} - F(\phi)\right], \tag{2.5.14}$$

$$P_{\phi} = \frac{1}{2}\dot{\phi}^2 - V(\phi) + \ddot{F}(\phi) + 2H\dot{F}(\phi) - (2\dot{H} + 3H^2)\left[\frac{1}{\kappa_*} - F(\phi)\right], \tag{2.5.15}$$

and the Klein-Gordon equation for the evolution of ϕ is:

$$\ddot{\phi} + 3H\dot{\phi} + \frac{\partial V(\phi)}{\partial\phi} = \frac{1}{2}\frac{\partial F}{\partial\phi}R, \tag{2.5.16}$$

with the Ricci scalar $R = 6(\dot{H} + H^2)$. For the potential $V(\phi)$ they use the one from the RP model (Eq. 2.5.10). More information on extended quintessence can be found in Pettorino and Baccigalupi (2008).

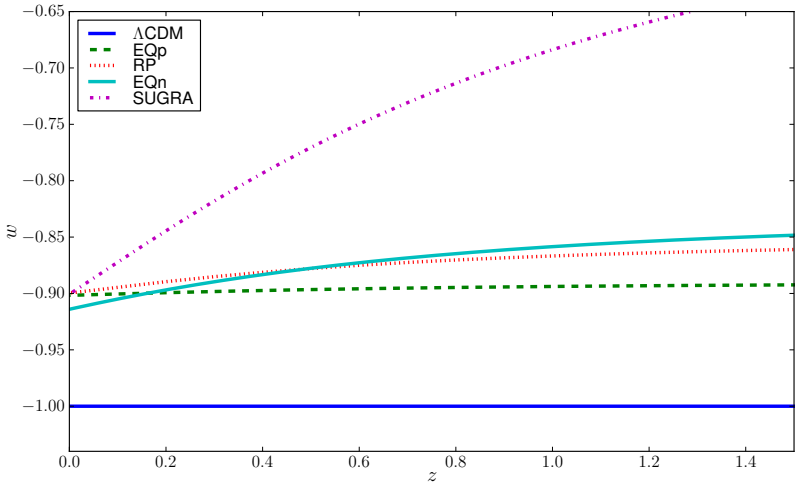

Figure 2.8: **The evolution of the w parameter for dark energy models.** The equation of state parameter is defined as $w \equiv P/\rho$. Figure data from de Boni et al. (2011).

A test for these models is the measurement of the Jordan-Brans-Dicke parameter from the perihelion shift of the planets (Brans and Dicke, 1961). This parameter is defined as:

$$\omega_{JBD} \equiv \frac{F(\phi)}{\left(\frac{\partial F}{\partial \phi}\right)^2}. \tag{2.5.17}$$

The Cassini mission yields a constraint of $\omega_{JBD} > 4 \times 10^4$ in the solar system (Bertotti et al., 2003). It is however possible that this parameter is not scale invariant; it may have a different value at larger scales. Acquaviva et al. (2005) found a lower limit of $\omega_{JBD} > 120$ on cosmological scales from WMAP and 2dF data.

The properties of the dark matter models are listed in Table 2.1. The ΛCDM model is based on the parameters in the 3-year data release of WMAP. The parameters are: $\Omega_m = 0.268$, $\Omega_b = 0.044$, $\Omega_\Lambda = 0.704$, $h = 0.704$. The values are also used for the quintessence models, with the exception of Ω_Λ. The cosmological constant has equation of state parameters $w_0 = -1$ and $w_a = 0$. The evolving dark energy models all have $w_0 = -0.9$ as this value gives the most dark energy influence while it is still allowed within the constraints of the WMAP data. The alpha parameter specifies the quintessence potential of Equation (2.5.9) or (2.5.10). For the extended quintessence models ω_{JBD} specifies the coupling constant, as it is related to ξ. The coupling is presented in this form for possible comparison to observational values.

2.6 Structure formation

This project is all about the evolution of structures in an expanding universe, so a qualitative description of structure formation is desirable. The starting point are the equations that describe the cosmic fluid. These are the continuity equation, the Euler equation and the Poisson equation, which will be explained in more detail in Chapter 3. For this description the equations need to describe the fluid in comoving coordinates. And in stead of the density, velocity and gravitational potential, these equations should describe the density perturbation δ, the peculiar velocity $\mathbf{v}$ and the perturbation potential ϕ. The equations are presented in

Model	α	w_{JBD}	w_0	w_a	σ_8
ΛCDM	-	-	-1.0	0.0	0.776
RP	0.347	-	-0.9	0.0564	0.746
SUGRA	2.259	-	-0.9	0.452	0.686
EQp	0.229	120	-0.9	0.0117	0.748
EQn	0.435	-120	-0.9	0.0805	0.729

Table 2.1: Parameters of the analysed dark energy models. α defines the quintessence potential; w_{JBD} is the Jordan-Brans-Dicke parameter (Eq. 2.5.17); w_0 and w_a are the closest matches to the parametrization constants of equation (2.5.1), determined with a χ^2 fit; and σ_8 is the normalization parameter for the power spectrum at the CMB. Numbers from de Boni et al. (2011) and Bos (2010).

this form in the lecture notes by R. van de Weygaert[1]. In the order given above, the equations are:

$$\frac{\partial \delta}{\partial t} + \frac{1}{a}\nabla \cdot \mathbf{v}(1+\delta) = 0 \tag{2.6.1}$$

$$\frac{\partial \mathbf{v}}{\partial t} + \frac{1}{a}(\mathbf{v}\cdot\nabla)\mathbf{v} + \frac{\dot{a}}{a}\mathbf{v} = -\frac{1}{a}\nabla\phi \tag{2.6.2}$$

$$\nabla^2\phi = 4\pi G a^2 \overline{\rho}\delta \tag{2.6.3}$$

These equations contain higher order terms like $\mathbf{v}(1+\delta)$ and $(\mathbf{v}\cdot\nabla)\mathbf{v}$ that make them hard to solve analytically. If we restrict ourselves to the early evolution of perturbations in the linear regime, these equations can be simplified. In the linear regime the density perturbations are very small $\delta << 1$. In addition, the velocities are so small that matter can not cross a perturbation in a characteristic expansion time. These two conditions allow the higher order terms mentioned above to be dropped, to yield:

$$\frac{\partial \delta}{\partial t} + \frac{1}{a}\nabla \cdot \mathbf{v} = 0 \tag{2.6.4}$$

$$\frac{\partial \mathbf{v}}{\partial t} + \frac{\dot{a}}{a}\mathbf{v} = -\frac{1}{a}\nabla\phi \tag{2.6.5}$$

$$\nabla^2\phi = 4\pi G a^2 \overline{\rho}\delta \tag{2.6.6}$$

The divergence of the Euler equation is taken to find a new equation:

$$\frac{\partial}{\partial t}\nabla\cdot\mathbf{v} + \frac{\dot{a}}{a}\nabla\cdot\mathbf{v} = -\frac{1}{a}\nabla^2\phi. \tag{2.6.7}$$

When the linear continuity equation and the Poisson equation are combined with this one, it results in an equation that describes the evolution of density perturbations:

$$\frac{\partial^2\delta}{\partial t^2} + 2\frac{\dot{a}}{a}\frac{\partial\delta}{\partial t} = 4\pi G\overline{\rho}\delta. \tag{2.6.8}$$

In words, this equation describes how the acceleration of the growth of the perturbation depends on the gravitational force due to the perturbation, but also how it decelerates due to

[1]These notes can be downloaded from his website at:
`http://www.astro.rug.nl/~weygaert/tim1publication/lss2009/lss2009.linperturb.pdf`

the expansion of the universe through the so called 'Hubble drag' term, which is the second term on the left side. Rewritten, and by substituting the background density with Ω_m from Equation (2.3.5), this becomes

$$\ddot{\delta} + 2H\dot{\delta} = \frac{3}{2}H^2\Omega_m\delta. \tag{2.6.9}$$

The form of this equation depends on the cosmology of the universe. In the case of an Einstein-de Sitter universe, the scale factor grows as $a \propto t^{2/3}$, which means $H \propto 2/(3t)$ (see Ryden, 2003). Consequently the equation to be solved then has the following form:

$$\ddot{\delta} + \frac{4}{3t}\dot{\delta} - \frac{2}{3t^2}\delta = 0. \tag{2.6.10}$$

The solution for this equation is in the form of a power law and consists of two parts.

$$\delta(t) \approx D_1 t^{2/3} + D_2 t^{-1} \tag{2.6.11}$$

The term with D_1 is usually called the growing mode, and the D_2 term the decaying mode. With increasing time, the decaying mode becomes negligible. Hence density perturbations grow according to

$$\delta(t) \propto t^{2/3} \propto a(t) \tag{2.6.12}$$

in the linear regime. This evolution is not valid for nonlinear overdensities where $\delta \gtrsim 1$.

The second important epoch for structure formation is the one where dark energy completely dominates, which will happen in the far future. In this case, the Hubble parameter becomes the constant H_0, because all other components in Equation (2.3.9) vanish with increasing $a(t)$. For the same reason, the matter density term can be dropped from right hand side of Equation (2.6.9) to yield

$$\ddot{\delta} + 2H_0\dot{\delta} = 0. \tag{2.6.13}$$

The solution to this equation can simply be found by integrating the solution for $\dot{\delta}$. This solution has an exponential term and an integration constant

$$\delta(t) = C_1\, e^{-2H_0 t} + C_2. \tag{2.6.14}$$

Obviously, the inverse exponential term will quickly vanish with time, independent of the values for the constants C_1 and C_2. With only a constant term left, the growth of perturbations is halted and they are frozen in this state. It will take a long time before the dark energy will completely dominate our universe, so this scenario will not have to be considered in studies of the past evolution of structures.

The general solution for the structure growth Equation (2.6.9) was given by Heath (1977). Neglecting the decaying mode solution, i.e.

$$\delta(t) = D(z)\delta_0, \tag{2.6.15}$$

the linear growth factor as a function of redshift is given by

$$D(z) = \frac{5\Omega_{m,0}H_0^2}{2}H(z)\int_z^\infty \frac{1+z'}{H(z')^3}dz'. \tag{2.6.16}$$

This growth factor depends on the cosmological model through both the relation between redshift and time and the Hubble parameter.

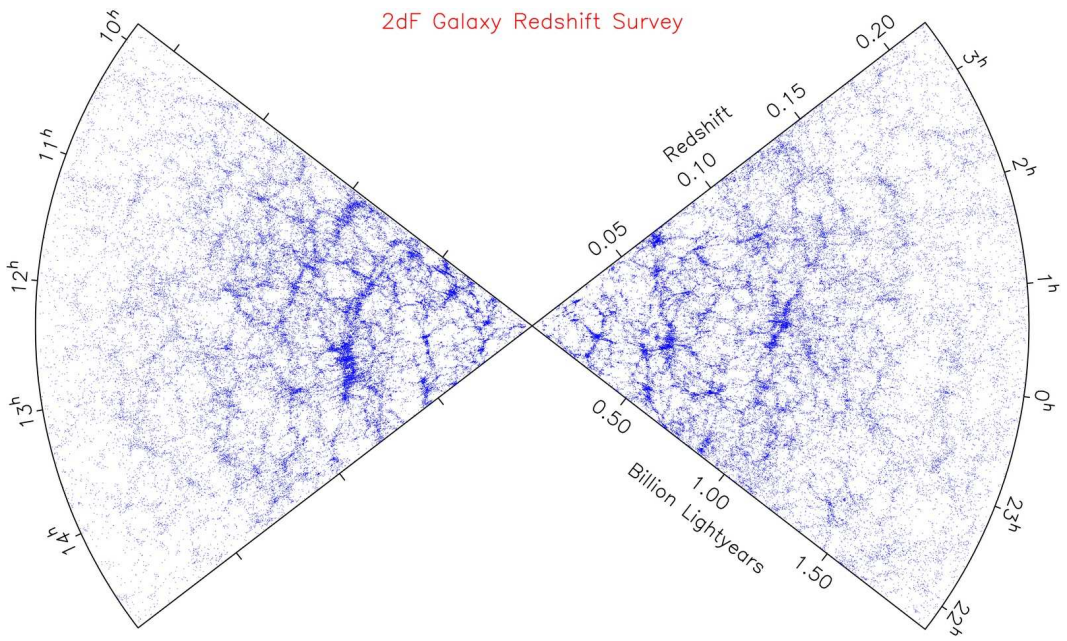

Figure 2.9: **The cosmic web.** Figure from Colless et al. (2003).

At some point the evolution of density perturbations becomes nonlinear. The density contrast becomes too high and the matter flows are influenced by tidal forces. The structures seen today are all formed in the nonlinear regime. In the regions between two underdensities the matter flows meet up. This results in a high density that prevents the matter flows to continue in a straight line. These regions then become walls and filaments. The matter flows along these walls and filaments towards the higher overdensities where clusters start to form. The clusters, filaments, walls and voids together form the cosmic web that is observed in galaxy redshift surveys like 2dF (Figure 2.9). The cosmic web continues to evolve, increasing the overdensities of clusters and underdensities of voids. In the process some clusters, filaments or voids may merge, increasing the density contrast even further.

Chapter 3

Lagrangian reconstruction: MAK

Eulerian vs Lagrangian. When we think about movements and dynamics, we usually choose a restframe and study the motions with respect to this frame. This is the Eulerian way of studying dynamics. Complementary to this is the Lagrangian way. In Lagrangian studies we look at the changes that any small volume element (a test particle) undergoes while it is moving through space. We track these particles by their initial position $\mathbf{q}$. For example, in the Eulerian view of fluid dynamics, we may see that at a certain point the fluid flows from right to left, and that the density of the fluid is higher on the right side than on the left. In the Lagrangian view, we would see that the coordinates $\mathbf{x}$ of our test particle are changing, and that the particle is expanding in the process. In this chapter we will mostly take the Lagrangian point of view.

3.1 Lagrangian perturbation theory

The equations of motion for a general fluid are respectively the Poisson equation, the Euler equation and the continuity equation. The Eulerian form of these equations is:

$$\frac{\partial \rho}{\partial t} = -\rho \nabla \cdot \mathbf{v} \tag{3.1.1}$$

$$\frac{\partial \mathbf{v}}{\partial t} = -\frac{\nabla p}{\rho} - \nabla \Phi \tag{3.1.2}$$

$$\nabla^2 \Phi = 4\pi G \rho \tag{3.1.3}$$

The continuity equation governs the conservation of mass by compensating the density in a volume element for in- and outflow of matter. The Euler equation shows the change in velocity of a test particle moving in a gravitational potential Φ, influenced by the pressure from its surroundings. Finally, the Poisson equation describes the gravitational potential corresponding to a mass distribution ρ. The Poisson and continuity equations are rather straightforward, so we will focus on the Euler equation. In cosmological simulations we work with a pressureless medium (dark matter), so the pressure term in the Euler equation is discarded. Now we want to write it in Lagrangian form, which translates into the use of the Lagrangian derivative:

$$\frac{d}{dt} = \frac{\partial}{\partial t} + (\mathbf{v} \cdot \nabla). \tag{3.1.4}$$

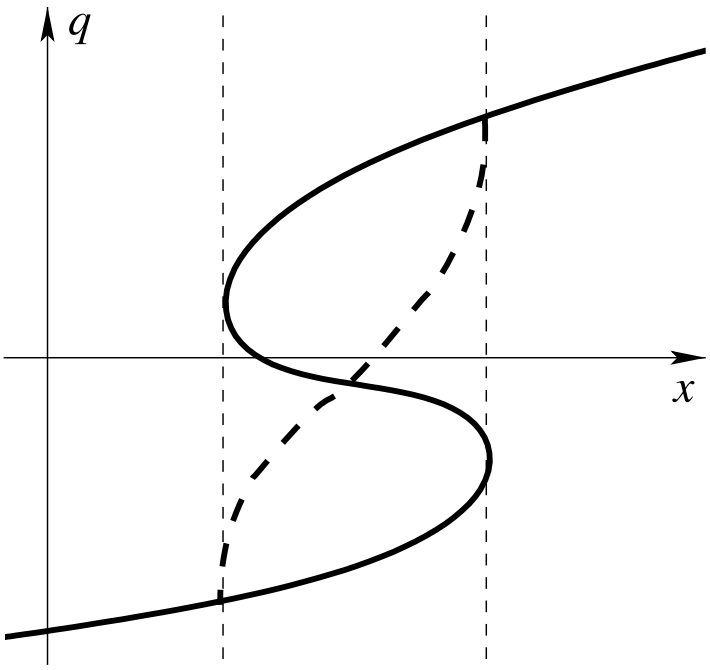

Figure 3.1: **Multistreaming in the Zel'dovich approximation.** This graph shows the initial (Lagrangian) position (**q**) as a function of the final (Eulerian) position (**x**) in a high density region. Multistreaming happens when the Zel'dovich approximation is used beyond the linear regime. In a multistreamed region, multiple **q**-positions are mapped to the same **x**-position. Figure from Brenier et al. (2003)

The additional term $\mathbf{v} \cdot \nabla$ is caused by the fact that we do not use a fixed coordinate system in the Lagrangian form. When there is a quantity that does not explicitly depend on time, but does depend on the spatial coordinates, measured by ∇, and if these coordinates change with time, i.e. there is a velocity $\mathbf{v}$, that quantity changes with time too. The Euler equation in Lagrangian form becomes:

$$\frac{\partial \mathbf{v}}{\partial t} + (\mathbf{v} \cdot \nabla)\mathbf{v} = -\nabla\Phi. \tag{3.1.5}$$

In Lagrangian perturbation theory we study the mapping of the Lagrangian coordinates $\mathbf{q}$ to their Eulerian coordinates $\mathbf{x}$ in a model of our universe. This is done in a Lagrangian way, because the fluid equations can more easily be solved. The map can be written as an ordered sequence of moments of displacement,

$$\mathbf{x}(\mathbf{q}, t) - \mathbf{q} = \mathbf{x}^{(1)}(\mathbf{q}, t) + \mathbf{x}^{(2)}(\mathbf{q}, t) + \mathbf{x}^{(3)}(\mathbf{q}, t) + \cdots, \tag{3.1.6}$$

where

$$1 > \left|\frac{\partial \mathbf{x}^{(1)}}{\partial \mathbf{q}}\right| > \left|\frac{\partial \mathbf{x}^{(2)}}{\partial \mathbf{q}}\right| > \left|\frac{\partial \mathbf{x}^{(3)}}{\partial \mathbf{q}}\right| > \cdots. \tag{3.1.7}$$

Each increasing order of complexity allows one to more accurately model the development of increasingly nonlinear structures. In the next section, a first order approximation of Lagrangian perturbation theory is explained in the form of the Zel'dovich formalism. After that we will move on to more advanced Lagrangian theories.

3.2 Zel'dovich

The Zel'dovich approximation was one of the first methods that explored the Lagrangian point of view in cosmology. It is a linear theory that describes the evolution of perturbations

in the early universe. The positions of particles evolve like

$$\mathbf{x}(t) = a(t)\mathbf{q} + D(t)\mathbf{p}(\mathbf{q}), \tag{3.2.1}$$

where $\mathbf{q}$ is the initial position and the cosmological expansion is represented by $a(t)$. The initial displacement vector at a given location is $\mathbf{p}(\mathbf{q})$, an $D(t)$ is the global growth rate of these displacements , i.e. the linear perturbation growth factor. These displacements are related to the linear velocity potential ϕ, but may also be written in terms of the gravitational potential Φ:

$$\mathbf{p}(\mathbf{q}) = \nabla\phi = \frac{2}{3H^2a^3}\nabla\Phi. \tag{3.2.2}$$

We can study the deformation of a small region around $\mathbf{q}$ by taking the derivative:

$$J_{ij} = \frac{\partial \mathbf{x}_i}{\partial \mathbf{q}_j} = a(t)\delta_{ij} + D(t)\frac{\partial \mathbf{p}_i}{\partial \mathbf{q}_j}. \tag{3.2.3}$$

This is the Jacobian matrix and can be diagonalised by using its principal axes as the coordinate system. The matrix then takes the form

$$J_{ij} = \delta_{ij}(a(t) - \lambda_i D(t)). \tag{3.2.4}$$

Here, the the eigenvalues λ of J_{ij} are sorted by size. Because mass is preserved, we can use this change in volume from the deformation to calculate the density at a certain point as

$$\rho(\mathbf{q}, t) = \frac{\rho_0 a(t)^3}{[a(t) - \lambda_1(\mathbf{q})D(t)][a(t) - \lambda_2(\mathbf{q})D(t)][a(t) - \lambda_3(\mathbf{q})D(t)]}. \tag{3.2.5}$$

In a collapsing region the density becomes infinite when $a(t) - \lambda_1 D(t) = 0$. Evolution should be stopped when this happens, to prevent orbit crossing. Orbit crossing is defined as the occurrence of an intersection of the trajectories of particles. A region where orbit crossing has occurred is called a multistream region (Figure 3.1). Multistream regions develop in the Zel'dovich approximation, because there is no mechanism to stop the movement of colliding particles. This means that density in a multistream region will decrease after the orbit crossing, because the particles are moving away in opposite directions. This is unphysical behaviour, so any multistream regions that develops should not be considered in the analysis. By keeping track of the sign of the λ values, one can determine which particles have undergone orbit crossing and should be excluded. The accuracy of this model can be robustly tested by calculating the force due to the gravitational potential from the particle distribution after a certain time. The acceleration due to this force can be compared to the acceleration that the particle has due to Equation (3.2.1).

3.3 Adhesion

The adhesion model provides a solution to the multistreaming problem of the Zel'dovich approximation. Adhesion is an analytical model based on hydrodynamics. It does not simulate particles that move in a gravitational potential, but it provides a set of hydrodynamical equations and solutions that are valid everywhere. We already saw the equations of motion for a general fluid in Section 3.1. Now we want to write the Euler Equation (Eq. 3.1.5) in

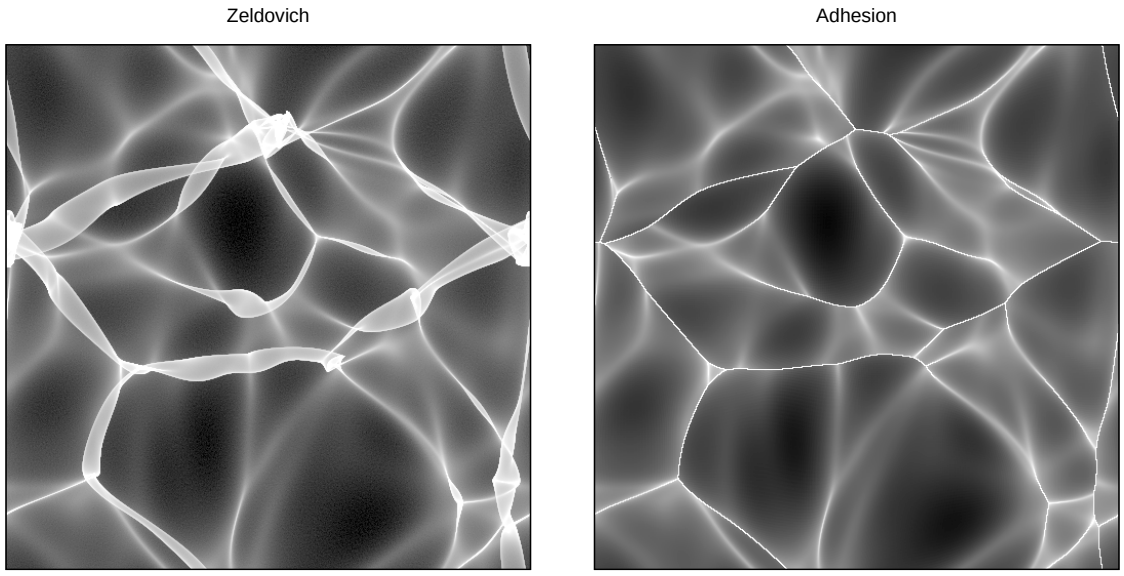

Figure 3.2: Comparison of Zel'dovich approximation and adhesion. The models were evolved in two dimensions according to the Zel'dovich approximation and adhesion. Multistreaming has occurred in the Zel'dovich model. The viscosity in the adhesion model prevents multistreaming and filaments are formed. The models are equal in low density regions and only differ where multistreaming has occurred. Image courtesy of Hidding et al. (2011).

a form where the linear growth factor $D(t)$ is used as the time parameter. In this comoving form it will be easier to use for cosmological purposes. The comoving velocity

$$\mathbf{u} = \frac{d\mathbf{x}}{dD} \tag{3.3.1}$$

is introduced in the Euler Equation by substituting:

$$\mathbf{v} = a\frac{d\mathbf{x}}{dt} = a\frac{dD}{dt}\frac{d\mathbf{x}}{dD} = a\dot{D}\mathbf{u}. \tag{3.3.2}$$

After the substitution the equation is rewritten to find:

$$\frac{\partial \mathbf{u}}{\partial D} + (\mathbf{u}\cdot\nabla)\,\mathbf{u} = -\frac{1}{\left(a\dot{D}\right)^2}\left(b\mathbf{u} + \nabla\Phi\right), \tag{3.3.3}$$

where $b\mathbf{u}$ is a rest term containing all linear a and D terms that are introduced by going to a comoving frame. In this form, it can easily be appreciated that the Euler equation for the Zel'dovich approximation becomes

$$\frac{\partial \mathbf{u}}{\partial D} + (\mathbf{u}\cdot\nabla)\,\mathbf{u} = 0. \tag{3.3.4}$$

This result can also be obtained by calculating

$$\mathbf{u} = \frac{d\mathbf{x}}{dD} = \frac{d}{dD}\left[a(t)\mathbf{q} + D(t)\mathbf{p}(\mathbf{q})\right] = \mathbf{p}(\mathbf{q}), \tag{3.3.5}$$

which is constant with respect to $D(t)$.

After this coordinate transformation, the adhesion model introduces an additional term for viscosity in the Euler equation to prevent multistreaming:

$$\frac{\partial \mathbf{u}}{\partial D} + (\mathbf{u} \cdot \nabla)\,\mathbf{u} = \nu \nabla^2 \mathbf{u}. \tag{3.3.6}$$

This equation is called Burgers' equation and was first used for large scale structure studies by Gurbatov and Saichev (1984). Of course, the viscosity should not prevent the free streaming of the dark matter fluid. Hence, the viscosity is taken to the inviscid limit: $\nu \to 0$. This means that the viscosity only 'activates' when the gradient of the velocity is infinite. This only happens when a multistream region is developing.

Burgers' equation has an analytical solution when the velocity has a potential form: $\mathbf{u} = -\nabla\Phi$. The solution is

$$\mathbf{u}(\mathbf{x}, D) = \frac{\int_{-\infty}^{\infty} \frac{\mathbf{x}-\mathbf{q}}{D} \exp\left[G/2\nu\right]}{\int_{-\infty}^{\infty} \exp\left[G/2\nu\right]}, \tag{3.3.7}$$

where we have extracted the parameter $G(\mathbf{x}, \mathbf{q}, D) = \Phi_0(\mathbf{q}) - (\mathbf{x} - \mathbf{q})^2/2D$. Φ_0 is the initial potential for our velocity. In the inviscid limit this rather difficult solution can be numerically calculated with the steepest descend method. It boils down to calculating the global maximum:

$$\Phi(\mathbf{x}, D) = \underset{\mathbf{q}}{max} \left[\Phi_0(\mathbf{q}) - \frac{(\mathbf{x} - \mathbf{q})^2}{2D} \right]. \tag{3.3.8}$$

This maximum can easily be found by lowering the parabola $\frac{(\mathbf{x}-\mathbf{q})^2}{2D}$ onto the potential $\Phi_0(\mathbf{q})$. The point where the parabola touches the potential is the $\mathbf{q}$ coordinate of the global maximum. In the linear regime, when $D \ll 1$, the parabola is very thin, and always touches the potential at a point $\mathbf{q}$ close to the value of $\mathbf{x}$. However, when D gets bigger and the parabola gets wider, it can not descend into deepest well of the potential anymore. The parabola will then touch the potential at two points on the rim of the well. The whole range of $\mathbf{q}$ in between is then mapped to a single value of $\mathbf{x}$, i.e. a shock has formed at $\mathbf{x}$.

In this case, where a region is completely collapsed in one direction, a thin sheet of infinite density is formed. This seems unphysical, but the sheet still has a finite mass and surface density, so it has a real potential. If the sheet also collapses in the other directions, it becomes a line or a point of infinite density but finite mass. With the multistreaming problem solved, the adhesion approximation gives much more realistic results. Compared to N-body simulations with the same initial conditions, the adhesion approximation can accurately reproduce statistical properties like the cluster mass function (Sathyaprakash et al., 1995). Minor drawbacks are that the positions where adhesion forms structures do not exactly coincide with the corresponding structures in the N-body simulation, and that it does not produce small scale structures.

3.4 The Monge-Ampère-Kantorovitch reconstruction

3.4.1 The MAK problem

The Monge-Ampère-Kantorovitch problem is a nonlinear Lagrangian approach to reconstructing the orbits of galaxies. By finding out where the matter of a galaxy came from, we can obtain an approximation of its current velocity. This velocity can be used to study the dynamics of galaxies in the cosmic web, or to extract the cosmological redshift from the total redshift to obtain a more accurate distance measurement. Alternatively, the reconstructed displacements of mass can be used in Lagrangian studies, e.g. to find the shapes of cosmic structures. We will use the MAK reconstruction to do a Lagrangian analysis of void shapes, a concept first introduced by Lavaux and Wandelt (2010).

The MAK reconstruction requires the current mass distribution of either galaxies or dark matter as input and assumes a uniform initial mass distribution. The goal of the MAK reconstruction is to find the map $\mathbf{q} \rightarrow \mathbf{x}$ for the optimal transportation of mass from the initial position $\mathbf{q}$ to the final position $\mathbf{x}$, or vice versa. For our reconstruction we must assume that the map is convex, which essentially means that any point $\mathbf{q}$ cannot be mapped to more than one point $\mathbf{x}$. This Lagrangian map should be of potential form, so we can write

$$\mathbf{x}(\mathbf{q}) = \nabla_{\mathbf{q}} \Phi(\mathbf{q}). \tag{3.4.1}$$

Well known examples that satisfy these conditions are the Zel'dovich approximation (before multistreaming) and the adhesion model. In reality our assumption is not valid in multistream regions like filaments and clusters, but it will allow us to find a unique reconstruction. The error introduced by falsely matched particles in these regions is small, since the particles in these high density regions are close together.

Let us consider the physics of the reconstruction. When we move particles from their initial to their final positions, the mass must be conserved. We can write this in an equation as:

$$\overline{\rho} d^3\mathbf{q} = \rho(\mathbf{x}) d^3\mathbf{x}, \tag{3.4.2}$$

where $\overline{\rho}$ is the initial uniform density field, and $\rho(\mathbf{x})$ the prestent one. In terms of the Jacobian matrix $\mathbf{J}$ this is:

$$\det(\mathbf{J}) = \det(\nabla_{\mathbf{q}} \mathbf{x}) = \frac{1}{\rho(\mathbf{x})}. \tag{3.4.3}$$

Inserting the potential form of the Lagrangian map we get:

$$\det(\nabla_{\mathbf{q_i}} \nabla_{\mathbf{q_j}} \Phi(\mathbf{q})) = \frac{1}{\rho(\nabla_{\mathbf{q}} \Phi(\mathbf{q}))}. \tag{3.4.4}$$

We can apply the same steps to the inverse Lagrangian map to obtain the same equation in a more suitable form. The inverse Lagrangian map is

$$\mathbf{q}(\mathbf{x}) = \nabla_{\mathbf{x}} \Theta(\mathbf{x}). \tag{3.4.5}$$

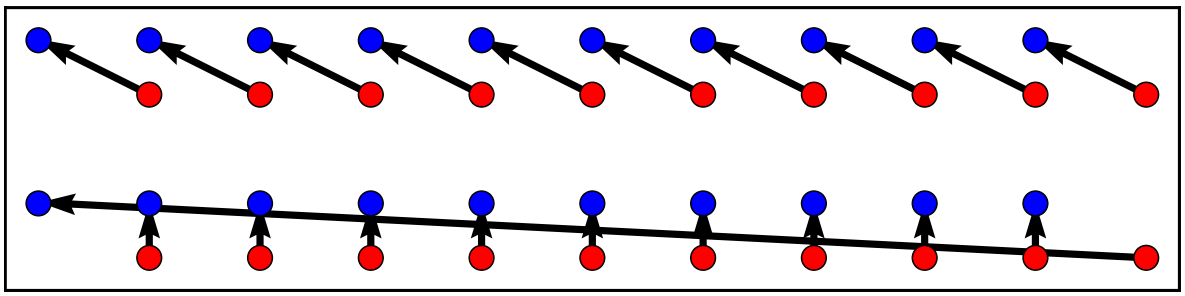

Figure 3.3: **A one dimensional reconstruction to illustrate the meaning of the cost function.** The row of final particles is the same as the row of initial particles, but displaced by a distance of *one* to the left. For the purpose of this illustration the initial and final rows were separated by a vertical displacement, but the horizontal distance is the only dimension considered in the reconstruction. Both displayed solutions are optimal for a linear cost function, but only the top one is optimal for the quadratic cost function.

It has the same properties as the Lagrangian map. Therefore, none of our assumptions for this map are lost. Following the same procedure with this map, we obtain the equation:

$$\det(\nabla_{\mathbf{x_i}} \nabla_{\mathbf{x_j}} \Theta(\mathbf{x})) = \rho(\mathbf{x}), \tag{3.4.6}$$

which is the Monge-Ampère equation. The result of the MAK reconstruction must satisfy this equation.

With our initial assumption of convexity, the Monge-Ampère equation has a unique solution. Solving this equation is equivalent to solving the *optimal mass transportation problem* posed by Monge (1781). He described how one could optimise the transportation of mass by minimising the total cost of the transportation. He used the transport distance as the cost function, but one can chose any suitable function for the cost of the transportation. In 1942 Kantorovich proved that the displacements of masses must be potential for the transport to be optimal. He also provided a method to find the optimal displacements for any cost function. This in the Monge-Kantorovitch problem. For our purposes we have to use the quadratic distance as the cost function for the transportation (see Frisch et al., 2002, and references therein). In other words, the integral

$$I = \int \frac{1}{2} \left|\mathbf{x}(\mathbf{q}) - \mathbf{q}\right|^2 \, \overline{\rho} \, d^3\mathbf{q} \tag{3.4.7}$$

must be minimal. The map of $\mathbf{q} \rightarrow \mathbf{x}$ that minimizes this integral is the unique solution to the Monge-Ampère Equation (3.4.6) (a formal proof can be found in Benamou and Brenier, 2000). The Monge-Ampère-Kantorovitch (MAK) problem is finding this minimal map that satisfies the Monge-Ampère equation. In our discrete case this integral is replaced by a sum.

$$I = \frac{1}{2}\overline{\rho} \sum_{i=1}^{N} \left|\mathbf{x}_{j(i)} - \mathbf{q}_i\right|^2 \tag{3.4.8}$$

We need to find the discrete map $j(i)$ that minimises this sum. The Auction algorithm has been developed by Bertsekas (1988) to solve the MAK problem in the discrete case.

A small test case is drawn in Figure 3.3 to illustrate the meaning of the cost function. This arrangement can be reconstructed in two ways: all 10 initial particles are matched to the final particle that is 1 position to their right; or all except the first initial particle are matched to the final one at their own coordinate, but the first initial particle must then be matched to the last final particle at a distance 10. When the cost function is linear, both solutions are optimal, since $I_1 = \sum_{i=1}^{10} 1 = 10$ equals $I_2 = 10 + \sum_{i=2}^{10} 0 = 10$. But the quadratic cost function favours many small displacements over one large displacement. This is also what one would expect to happen in structure formation. For the quadratic cost function the total costs are $I_1 = \sum_{i=1}^{10} 1^2 = 10$ and $I_2 = 10^2 + \sum_{i=2}^{10} 0 = 100$. Consequently, only the top solution is optimal, which is hardly surprising since this method was designed to produce a unique reconstruction.

3.4.2 The Auction algorithm

This section provides a short description of the Auction algorithm that solves the assignment problem to produce the Monge-Ampère-Kantorovitch (MAK) reconstruction. The goal of the Auction algorithm is to find the mapping between two sets of data, in this case coordinates, that minimises the integral over a certain cost function. In our case the most suitable cost function is the square of the distance between the two points, because this cost function solves the Monge-Ampère Equation (3.4.6) (Benamou and Brenier, 2000). For this purpose the algorithm performs a virtual auction where one set of points are the **bidders** and try to buy the **objects** in the other set. The auction is done in rounds, because favourable objects receive bids from multiple bidders but can only be assigned to one of them, leaving the rest unassigned after this round. In subsequent rounds the unassigned bidders will bid on other objects. The following steps are done to make a reconstruction.

For each bidder that is not yet assigned, the two objects with the lowest cost need to be selected. The **cost** (C) is the amount a bidder (B) is willing to pay for an object (O). This cost depends on the cost function, i.e. the quadratic distance to the object, and on the price of the object. The **price** (p) of an object is the amount that has been paid for the object in a previous round. In the first round all objects have a price of zero. The cost of an object for a bidder is calculated with:

$$C(O, B) = f_c(O, B) + p(O, B_p) = (\mathbf{x}(O) - \mathbf{x}(B))^2 + p(O, B_p), \tag{3.4.9}$$

where f_c is the cost function and $p(O, B_p)$ is the price that was paid for the object by the previously assigned bidder (B_p). This calculation is done for all unassigned bidder-object combinations. For each bidder the two objects with the lowest cost are selected, the best object is marked as O_1, and the second best as O_2.

Each bidder next places a bid on its most desired object. The price p that bidder B is willing to pay depends on how favourable the best object is compared to the second best object, as well as on the price previously paid for this object,

$$p(O_1, B) = C(O_2, B) - C(O_1, B) + p(O_1, B_p). \tag{3.4.10}$$

Example: Table 3.1 lists the steps in the reconstruction of the three pairs of points drawn in Figure 3.4. The example is in one dimension, so only the horizontal distance is considered. The algorithm starts by calculating the costs for each bidder-object pair based on Equation (3.4.9). It then selects the best and second best objects for each bidder and calculates the height of the bid on the best object (Equation 3.4.10). In the first round all bidders place their bids on the closest object, because the prices $p(O_1, B_p)$ of all objects are zero. Bidder B_1 bids on object O_2 and gets the assignment because there are no other bidders. Bidders B_2 and B_3 both place bids on O_3, but B_3 wins because his second best object costs so much more. In round two B_2 is the only unassigned and thus active bidder. Because the price of object O_3 has been set to 3 in the previous round, B_2 now places a bid on O_2 which only costs 2 (1 for the distance and 1 for the price set by B_1). Because B_2 places a higher bid on O_2 than B_1 did in the previous round, it gets the assignment and B_1 is returned to the unassigned pool. In round three B_1 is the only active bidder. This round is more or less the same as the previous round as B_1 shifts its bid to O_1. With no previous bids on O_1, it immediately gets assigned and the reconstruction is complete.

O_1 and O_2 are the best and second best objects for this bidder respectively. Once all bids have been placed, we can start assigning objects to the highest bidders. The condition for assignment is that the bidder is willing to pay more for this object than the previously assigned bidder.

$$p(O_1, B) > p(O_1, B_p) \tag{3.4.11}$$

Each bidder B that meets this condition, gets the assignment to its preferred object O_1. The new price for this object now becomes the height of B's bid. The bidder B_p that was previously assigned to this object is returned to the unassigned pool. Note that for the first bidder this condition reduces to $C(O_2, B) - C(O_1, B) > 0$, which is always true. However, for the next bidder that also placed a bid on this object, the bid will be compared to the new price that was placed by this first bidder. When all bids have been processed, a new round starts for all bidders that are not assigned to an object, thus return to Equation 3.4.9.

We will obtain the optimal assignment by following this procedure until all bidders are assigned to a unique object. With the huge number of particles we typically work with in studies of the large scale structure, this procedure will take a very long time. Specifically, when there is only one particle left unassigned in a certain area, a single round of bidding will typically swap the assignment of another particle with this particle, leaving the other particle unassigned. There are endless combinations that must be investigated one after the other. The algorithm only progresses when an object that is not yet assigned becomes the most favourable for assignment.

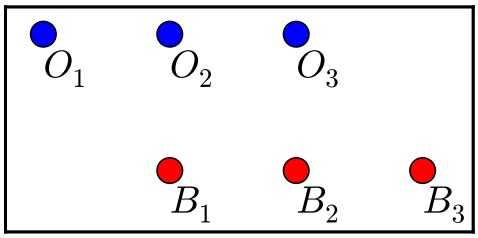

Figure 3.4: **Example.**

A solution to this problem is explained in Bertsekas. He suggests that the condition for assignment (Eq. 3.4.11) should be modified to increase the threshold for assignment by an

amount ϵ:

$$p(O_1, B) > p(O_1, B_p) + \epsilon. \tag{3.4.12}$$

As a result, the bidder can only acquire an object when he is willing to pay ϵ more than the previous bidder did. So each time an object is assigned to a new bidder, the cost of this object increases at least by an additional amount of ϵ. This will make objects that have not been assigned yet more attractive with respect to objects that have had multiple assignments.

The modification will not produce the optimal assignment of particles, but it provides a rough mold of the optimum. If we now start a new assignment with a lower value for ϵ, but keeping the obtained prices of the objects, we can obtain a new and more accurate assignment in much less computation time. This process can be repeated several times. If we set $\epsilon = 0$ for the final step we obtain our original condition (3.4.11) that will definitely result in the optimal mapping we are looking for. With a proper number of steps and good values of epsilon, this method will take less computation time than the unmodified algorithm described above.

This modification increases the efficiency of the algorithm, because the costs set in previous rounds will keep most bidders away from the most popular objects. The bidders that have less to spend can't afford to bid on these popular objects, and will immediately be directed towards less favourable, but less expensive objects. The least popular objects are now much easier to assign, reducing the computation time.

An additional speed-up can be achieved by reducing the problem of the last few assignments that are very hard to make. If we use the ϵ-method described above with multiple rounds, the first few rounds are not meant to have an accurate result. We can therefore simply terminate the calculation once we drop below a certain threshold of unassigned particles. The particles that remain unassigned will have a lower cost in the next round, making them more attractive. By reducing the threshold in each subsequent round, we will gain more accuracy when we need it.

	Round 1					Round 2					Round 3				
	C (Eq. 3.4.9)			$p =$ (Eq. 3.4.10)	As.	Cost			Bid	As.	Cost			Bid	As.
	O_1	O_2	O_3			O_1	O_2	O_3			O_1	O_2	O_3		
B_1	1	0	1	$1-0+0=1$	O_2					–	1	2	4	1	O_1
B_2	4	1	0	$1-0+0=1$	–	4	2	3	2	O_2					O_2
B_3	9	4	1	$4-1+0=3$	O_3					O_3					O_3

Table 3.1: **Auction example.** Listed for each round are: the costs for each bidder-object pair (Eq. 3.4.9); the height of the bid of each bidder on the object with the lowest cost (Eq. 3.4.10); and the assignments that are in place at the end of the round.

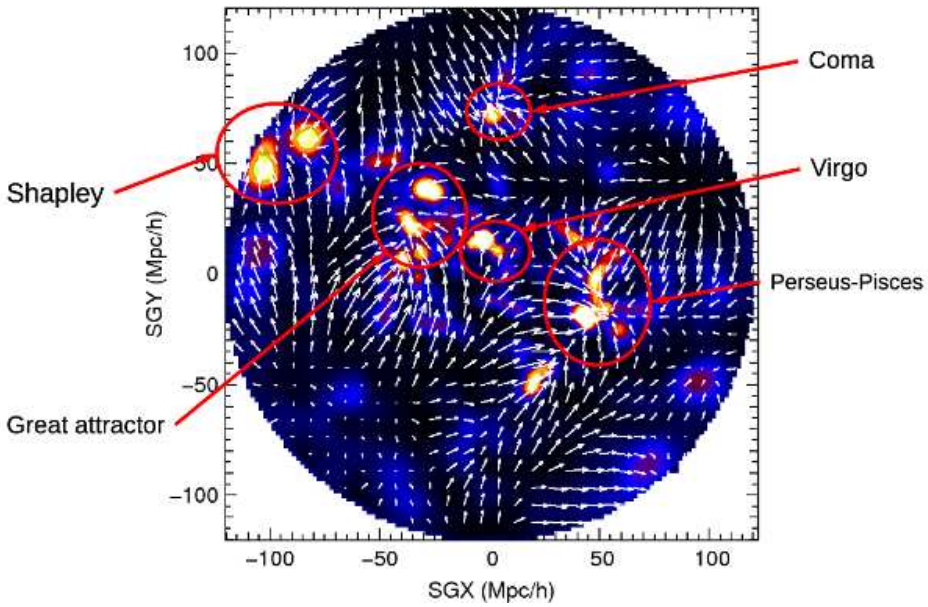

Figure 3.5: **A MAK reconstruction of the local universe.** The velocities in the local universe were reconstructed with MAK. Image from Lavaux (2010)

3.4.3 Applications

The MAK reconstruction has many applications in astronomy. Frisch et al. (2002) investigated the reconstruction of initial density perturbations. In a similar effort Sirko and Spergel (2005) reconstructed the primordial power spectrum with galaxies from the Sloan Digital Sky Survey. Mohayaee and Tully (2005) used MAK to constrain cosmological parameters and to reconstruct peculiar velocities of galaxies in a small galaxy redshift catalogue.

In a more recent effort, Lavaux (2010) use the MAK reconstruction method on the local universe. They made a reconstruction of the peculiar velocities in the local universe that is caused by the large clusters. For their data they used two catalogues: the Two-Micron All Sky Redshift Survey (2MRS; based on the 2MASS survey) and the Nearby Galaxy 3,000 km/s (NBG-3k) distance catalogue for more accurate data of galaxies with a low redshift. They did a three-dimensional reconstruction and extracted a thin slice around the supergalactic plane. This slice is displayed in Figure 3.5. It shows the full extent of the reconstruction, up to a distance of 100 Mpc, but survey is only complete up to ~ 60 Mpc. The reconstruction was extended to prevent boundary effects in the completely sampled area. This reconstruction of the orbits of galaxies gives an approximation of the velocity field in the local universe. MAK is better suited for these types of reconstructions than other Lagrangian techniques, because it reconstructs the velocities of the galaxies themselves, while other techniques reconstruct velocities on grid point. Moreover, the nonlinear approach of MAK makes it overall more accurate than linear reconstruction techniques. Finally, the only information required for a MAK reconstruction is the positions of galaxies. Where other methods need more, MAK can reconstruct orbits from positions only, assuming a uniform distribution initially.

3.4.4 Other reconstruction methods

There are other reconstruction methods with the same intention as MAK. The Zel'dovich-Bernoulli reconstruction is based on inverting the Zel'dovich approximation. It uses the current positions and velocities of galaxies and extrapolates the evolution back in time. This method works rather well in the linear regime, but the problem is that the current velocities are often unknown. Nusser and Dekel (1992) developed a method to approximate the velocities from the density field, but this extra step produces a highly inferior reconstruction, often with orbit crossing in the initial field that should be approximately uniform.

The Least Action reconstruction first introduced by Peebles (1989) is more similar to MAK. It assumes a uniform initial mass distribution and requires a current galaxy distribution as input. It then defines an action for the displacement of a certain galaxy to any initial position. The total action is then minimized by interchanging the reconstructed positions of two galaxies such that total action decreases. A disadvantage of this method is that the reconstruction is not always a unique solution, and with a number of possible results the reconstruction may end up in a local minimum in stead of a global one. The MAK reconstruction is much faster and it is guaranteed to be unique. However, it does not perform as well as the Least Action method in highly nonlinear regions (see Mohayaee and Tully (2005) for a comparison).

Chapter 4

Voids and dark energy

4.1 Voids

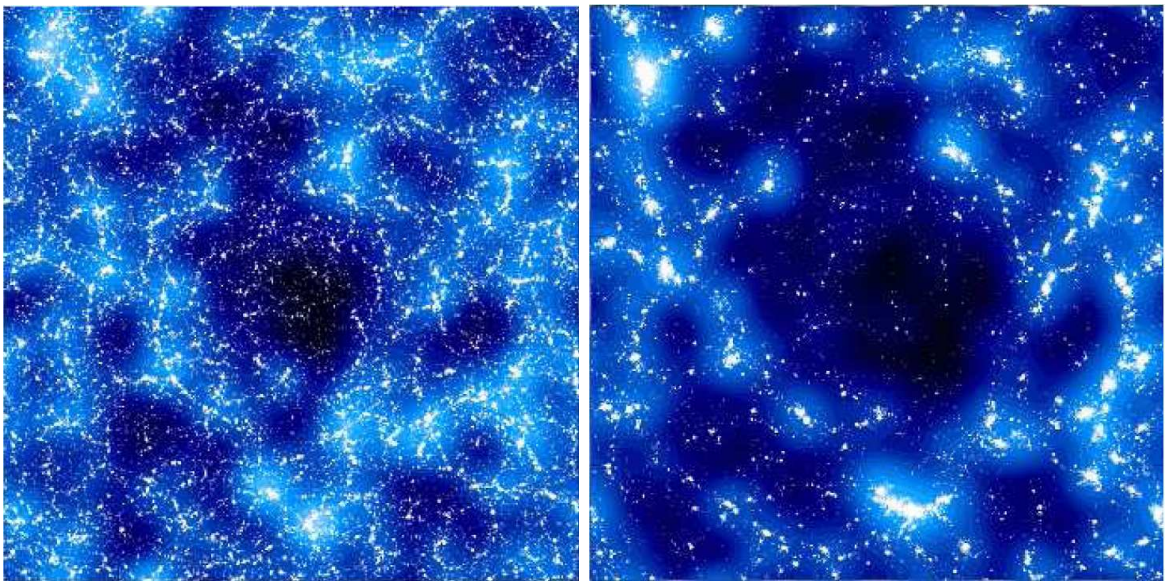

Figure 4.1: **A growing void.** Two snapshots of a void evolving in a ΛCDM simulation. The left panel is the void at $a(t) = 0.15$ and the right panel at $a(t) = 1$. Figure from van de Weygaert and Platen (2009).

A void is a vast empty region of space with a diameter of $20 - 50h^{-1}$ Mpc. They were first discovered in two independent redshift surveys by Gregory and Thompson (1978) and Joeveer et al. (1978). In their studies of dense structures in early redshift surveys of galaxies they discovered that the structures were seperated by large empty regions. In the first mentioned study these regions were called voids. This discovery resulted in more extended redshift surveys, which eventually led to conclusion that galaxy distribution forms a web-like structure composed of clusters, filaments and voids.

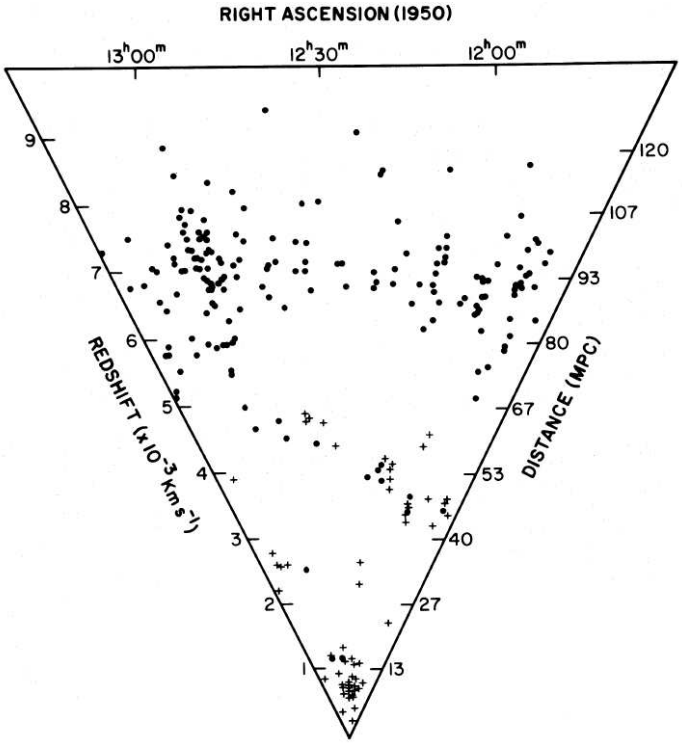

Figure 4.2: **An early observation of the Coma void by Gregory and Thompson (1978).**

The seeds for the formation of voids were tiny underdensities in the initial density field. Because the density is lower in these regions, the matter is pulled towards surrounding overdensities and vacates the underdense region (see Figure4.1). There is a continuous outflow of gas and dark matter as it is pulled into the filaments and clusters by gravity. The voids continue to grow in both size and underdensity, i.e. the density contrast between clusters and voids increases, as the high density structures around them undergo gravitational collapse (see figure 4.1). Because they are depleted from all gas, hardly any galaxies can form in these regions.

It appears that there is an hierarchical aspect to void evolution. A large underdense region consists of many small voids, separated by thin walls or filaments. There is a continuous outflow of matter along the filaments or walls into clusters, gradually reducing their size and density, until they become indistinguishable and the voids that they separated are essentially merged. A simulation of a void showing this behaviour is shown in the top row of Figure 4.3. It takes longer for substructure to completely disappear than the current age of the universe. The fainted substructures may not be visible in most observed voids, but it is probably still there. On the other hand, the walls and filaments that form the boundary may merge with other boundary structures, effectively causing the void in between to disappear. This is what happens in the bottom row of Figure 4.3. Such a void, that is collapsing in one direction but may be expanding in another, is called a pancake or filament void (see Figure 4.4). Whether a void is expanding or collapsing is extremely hard to observed. One needs dynamical information to separate the expanding voids from the collapsing ones. But at cosmological distances the redshift can not be used as a measure for velocity, so another method is required. We will do a Monge-Ampère-Kantorovitch reconstruction to obtain the necessary dynamical

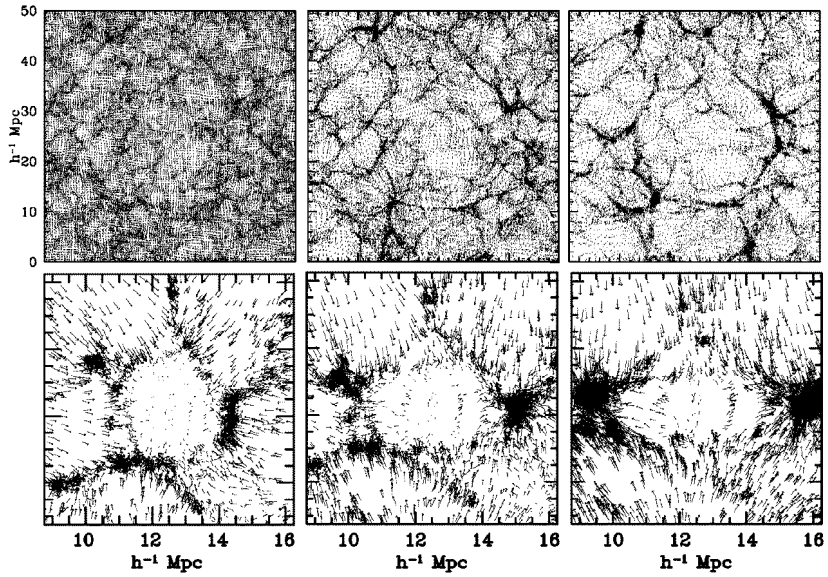

Figure 4.3: **Evolution of growing and collapsing voids.** In the top row a large, fragmented underdense region gradually empties. The substructure visible in the first panel gets fainter toward the last panel. The subvoids will merge as the void evolves, to eventually only leave the large void. In the bottom panel two filaments are merging, causing the void in between to disappear. Figure from van de Weygaert and Platen (2009).

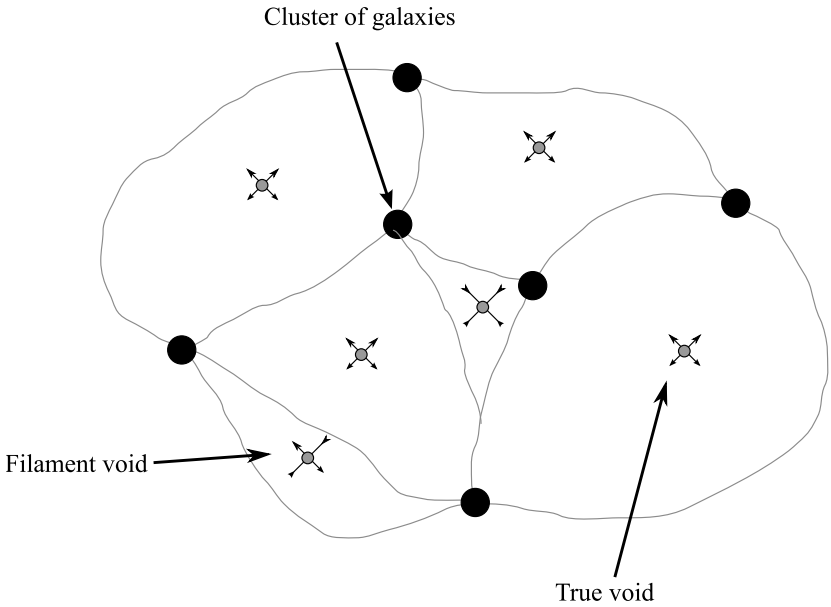

Figure 4.4: **A sketch of some types of voids.** True voids expand in all directions, while pancake voids collapse in one direction and filament voids are collapsing in two directions. The collapse is caused by the boundaries that are gravitationally attracted to each other, with a merger as the result. This figure from Lavaux (2010) shows the two possible types in a two dimensional space.

information and study the difference between these types of voids.

How empty voids are is still an open question. Observations do show a few stray galaxies in voids that do not contribute significantly to the density of the void (van de Weygaert et al., 2011). But voids may be filled with dwarf galaxies that are to faint to observe. This idea comes from N-body simulations that show there is a significant amount of dark matter left in

voids. In high resolution simulations of voids by Gottlöber et al. (2003), this dark matter is many clustered in small haloes. Only a few haloes are formed that are large enough to host galaxies with observable brightness. However, it is unknown whether dwarf galaxies actually form in these small haloes, leaving this question unsolved.

During their evolution voids are subject to tidal forces from the high density structures around them. They already start as non-spherical Gaussian perturbation that show some degree of alignment (Bond, 1987). Both this ellipticity and alignment are enhanced by the tidal forces. The tidal forces are the strongest towards large neighbouring clusters of galaxies. Thus the voids are stretched mostly in the direction of this cluster, such that their longest axis points towards the cluster. A neighbouring void will feel the tidal forces from the same cluster, causing the alignment between these voids to increase. These neighbouring voids are usually separated by a wall or filament connected to the cluster, so the long axis of the voids must to some degree also be aligned to these structures. These predicted shapes and alignments were indeed found by Platen et al. (2007) in N-body simulation.

In this project we study the evolution of the shapes of voids. The boundary and thus the shape of a void depends on the exact definition of a void. The matter density gradually increases when moving from the center of a void towards its boundaries. When we define the boundary as an isodensity surface, the void will have a very lumpy but more or less ellipsoidal shape. Alternatively, we can interpret the large scale structure as a cosmic foam, and allow voids to fill the entire volume, while their boundaries are infinitely thin. Such voids would have a smooth surface, but their shape can not be represented by a simple geometrical form. In addition, this method does not consider different density levels which may hold information on the shape of a void. In the next section we will discuss some void finders, each with its own definition of a void boundary.

4.1.1 Void finders

There are three classes of void finding algorithms: (i) searching for empty regions in a particle distribution; (ii) finding low density regions in a density field; and (iii) using dynamical information to find expanding regions. The first is used on observed galaxy distributions or on simulations that identify galaxy candidates. The second is better suited for a dark matter density field from a simulation, as it is more sensitive to small substructures. It can also be applied to a galaxy distribution by first converting it to a density field. The dynamical method is not widely used because it can not be applied to observations. However, a reconstruction method that can provide the dynamical information may be used for this class of void finders.

Most algorithms that find voids in a galaxy distribution try to identify empty regions of a certain shape (cubes, spheres, ellipsoids), e.g. Brunino et al. (2007). Some algorithms then take steps to deviate from this geometrical shape to make a better approximation of the true shape of the void. For example, Gottlöber et al. (2003) (spheres) and Müller et al. (2000) (cubes) place a single large object in each empty region, and then attach smaller objects (down to a certain limit) of the same shape to the surface of the larger one. Another possibility

is drawing many spheres in empty regions and merging overlapping spheres to obtain a void approximation. The 'voidfinder' of Hoyle and Vogeley (2002) divides the field into a grid. For each grid point they draw a sphere with the largest possible radius that leaves it empty. Then all overlapping spheres are merged to form an irregularly shaped void. In these methods it is of course possible to ignore galaxies below a certain mass or luminosity, as voids can contain some stray galaxies.

A similar merging scheme can be used for finding voids in a density field. In this case the spheres that are to be merged are drawn around local minima in the density field. The spheres are expanded until the mean density of the region it delimits, reaches a certain limit (e.g. Colberg et al. (2005)). In such merging schemes it is necessary to either use only rather large spheres or to set conditions for the merging. Otherwise two voids can be merged by small spheres that cross the border between both voids, resulting in strange shapes and sizes.

A very intuitive void finding technique that has been developed by Platen et al. (2007) is the Watershed Void Finder. The algorithm is analogous to the flooding of a landscape. A density field is first obtained from a particle distribution by the Delauney Tesselation Field Estimator (DTFE) from Schaap and van de Weygaert (2000). All local minima in the density field are than marked as sources for flooding. As water flows from the sources the level gradually rises, filling the underdense regions (basins). When the water hits a saddlepoint in the density field, two neighbouring basins can merge. A dam is erected at this point to prevent the merging. When the water level rises further, this dam is extended and new dams are erected to prevent any merging. When the field is completely flooded, all that remains is a web-like structure of dams. These are the boundaries of the voids. This technique is known in mathematical morphology as the Watershed Transform, which is the origin of the name Watershed Void Finder.

An example of a void finder that uses dynamics is the one by Hahn et al. (2007). They derive a gravitational potential from the density distribution and analyse the equations of motion for a test particle in this potential. From this they obtain the tidal field tensor T_{ij} at the position of the test particle. They classify voids as the regions where the eigenvalues of the tidal field tensor are all positive, i.e. the points that are gravitationally unstable. This last step is the same for void finding with MAK that we use in this project. Figure 4.5 shows how some of the mentioned void finders perform on a simulation.

4.2 Dark energy and voids

There have been many attempts in recent years to find observational evidence that can put constraints on the equation of state for dark energy. Suggested probes are, among others, the luminosity versus distance relation of supernovae type Ia, weak gravitational lensing and the mass function of galaxy clusters. A recent addition to this list by Park and Lee (2007) is the evolution of the shape of voids. Because voids are like huge bubbles in the cosmic foam, their shapes are determined by weak forces on large scales. In particular there are two counteracting forces that have a strong influence on the shapes of voids. On the one

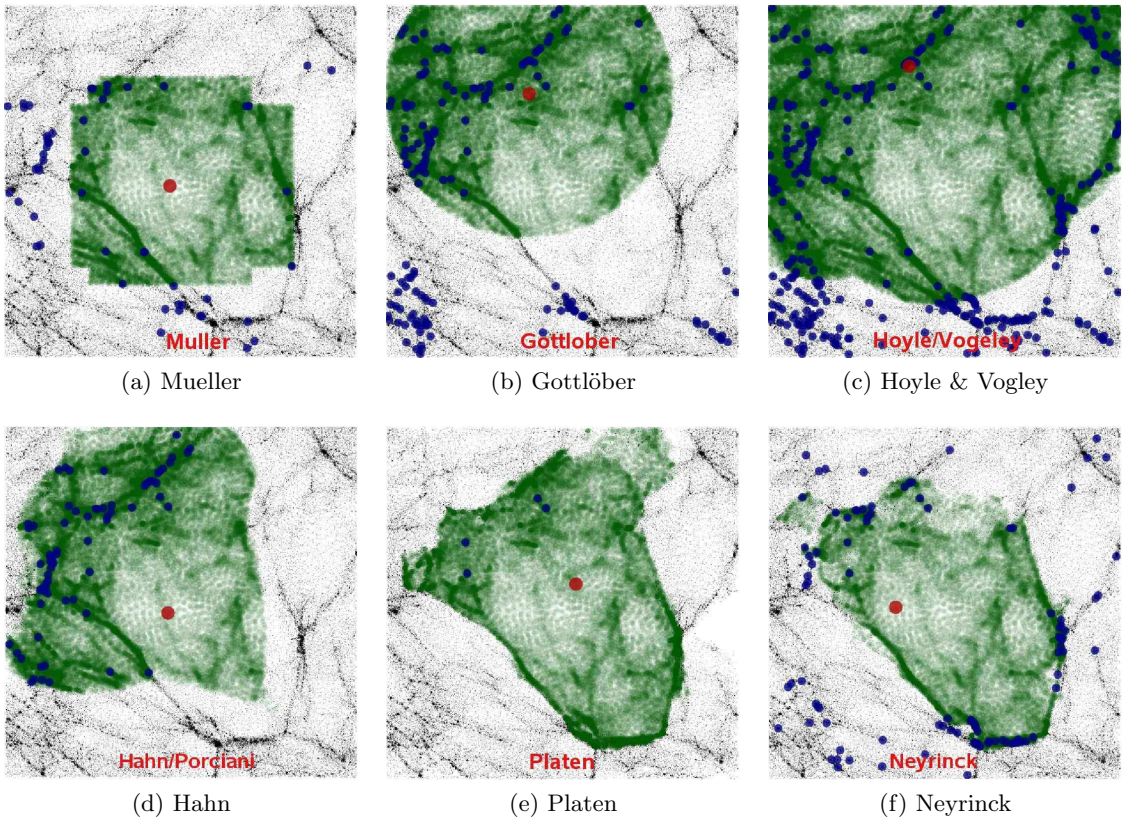

(a) Mueller (b) Gottlöber (c) Hoyle & Vogley

(d) Hahn (e) Platen (f) Neyrinck

Figure 4.5: **Various void finders.** The green region is the void found by the algorithm and the red dot is the associated center. The blue dots are galaxies embedded in the simulated dark matter background. Figures from Colberg et al. (2008).

hand we have the expanding universe. The stretching of space in and around the void will make it more spherical in shape, just like an oddly shaped balloon will get more spherical when it is blown up enough. On the other hand, we have shearing forces from massive galaxy clusters near a void. They will distort the shape of the void, resulting in a less symmetric and therefore more elliptical shape. Because dark energy influences the growth rate of structures, it also influences the void shapes through the shearing forces from these structures.

At the core of our analysis of void shapes is the displacement field, which we call $\mathbf{\Psi}$. It is simply the reconstructed displacement from the initial position $\mathbf{q}$ to the final position $\mathbf{x}$:

$$\mathbf{\Psi}(\mathbf{q}) \equiv \mathbf{x}(\mathbf{q}) - \mathbf{q} \tag{4.2.1}$$

You may recall from Section 3.4 that in the case of MAK this can be written in the more familiar potential form:

$$\mathbf{\Psi}(\mathbf{q}) = \nabla_{\mathbf{q}}\Phi(\mathbf{q}), \tag{4.2.2}$$

with $\nabla_{\mathbf{q}}$ the Lagrangian derivative of $\Phi(\mathbf{q})$. We define the tidal shear tensor as

$$\mathbf{T}_{i,j}(\mathbf{q}) = \frac{\partial \mathbf{\Psi_i}(\mathbf{q})}{\partial \mathbf{q}_j} = \frac{\partial^2 \Phi(\mathbf{q})}{\partial \mathbf{q}_i \partial \mathbf{q}_j}. \tag{4.2.3}$$

The Jacobian matrix is related to the tidal shear tensor $\mathbf{T}_{i,j}(\mathbf{q})$:

$$\mathbf{J}_{i,j}(\mathbf{q}) = \frac{\partial \mathbf{x_i}(\mathbf{q})}{\partial \mathbf{q}_j} = \frac{\partial(\mathbf{q}_i + \mathbf{\Psi_i}(\mathbf{q}))}{\partial \mathbf{q}_j} = \delta_{i,j} + \mathbf{T}_{i,j}(\mathbf{q}), \tag{4.2.4}$$

where $\delta_{i,j}$ is the Kroneker delta. Then we calculate the eigenvalues of the tidal shear tensor and sort them in descending order. These eigenvalues (λ_i) can be used for the shape analysis. The major axis length of the ellipsoid that approximates the void shape is $1 + \lambda_1$ and the minor axis length is $1 + \lambda_3$ (these are the eigenvalues of the Jacobian). These eigenvalues can also be used to calculate the density at a point $\mathbf{q}$:

$$\rho(\mathbf{q}) = \rho_0(\mathbf{q})\,|J_{i,j}| = \frac{\rho_0(\mathbf{q})}{(\lambda_1+1)(\lambda_2+1)(\lambda_3+1)}. \tag{4.2.5}$$

From this it is obvious that, if $\lambda_i > 0$ for all i, the region must be underdense and we are dealing with a void. When only $\lambda_1 > 0$ and $\lambda_2, \lambda_3 < 0$ the region may or may not be underdense. In this case the value of $\sum \lambda_i > 0$ can be used to determine whether a region is underdense.

The probability distribution of ellipticities of voids, as measured by the eigenvalues $\lambda_1 \geq \lambda_2 \geq \lambda_3$ of the tidal shear tensor T_{ij}, was derived by Doroshkevich (1970):

$$p(\lambda_1,\lambda_2,\lambda_3;\sigma_{R_L}) = \frac{3375}{\sqrt{5\pi}\sigma_{R_L}^6} \exp\left[-\frac{5\delta_\nu^2}{2\sigma_{R_L}^2} + \frac{15\delta_\nu(\lambda_1+\lambda_2)}{2\sigma_{R_L}^2}\right] \exp\left[\frac{15(\lambda_1^2+\lambda_1\lambda_2+\lambda_2^2)}{2\sigma_{R_L}^2}\right](\lambda_1-\lambda_2)(\lambda_2-\lambda_3)(\lambda_1-\lambda_3)\,. \tag{4.2.6}$$

In words, $p(\lambda_1,\lambda_2,\lambda_3;\sigma_{R_L})$ is the probability to find the values λ_1, λ_2 and λ_3, as a function of σ_{R_L}. To evaluate the probabilities for void shapes it is convenient to define the shape parameters

$$\mu = \left(\frac{1+\lambda_2}{1+\lambda_1}\right)^{1/2}, \quad \nu = \left(\frac{1+\lambda_3}{1+\lambda_1}\right)^{1/2}, \quad \varepsilon = 1-\nu. \tag{4.2.7}$$

The prolateness is measured by μ and the aspect ratio for the major an minor axes ν is used to define the ellipticity ε. In addition we define the parameter $\delta = \lambda_1+\lambda_2+\lambda_3$ that measures the local underdensity. The above probability distribution can then be written as a function of the shape parameters μ and ν and δ by substituting:

$$\lambda_1(\mu,\nu) = -\frac{\mu^2+\nu^2-(\delta+2)}{\mu^2+\nu^2+1} \tag{4.2.8}$$

$$\lambda_2(\mu,\nu) = -\frac{1+\nu^2-(\delta+2)\mu^2}{\mu^2+\nu^2+1} \tag{4.2.9}$$

$$\lambda_3(\mu,\nu) = -\frac{1+\mu^2-(\delta+2)\nu^2}{\mu^2+\nu^2+1} \tag{4.2.10}$$

The distribution function of void ellipticities can be obtained by calculating:

$$p(1-\varepsilon;\sigma_{R_L}) = p(\nu;\sigma_{R_L}) = \int_{\mu=\nu}^{1}\int_{\delta=0}^{\infty} p(\lambda_1(\mu,\nu),\lambda_2(\mu,\nu)|\delta_\nu;\sigma_{R_L})\frac{4(\delta_\nu-3)^2\mu\nu}{\mu^2+\nu^2+1}d\mu. \tag{4.2.11}$$

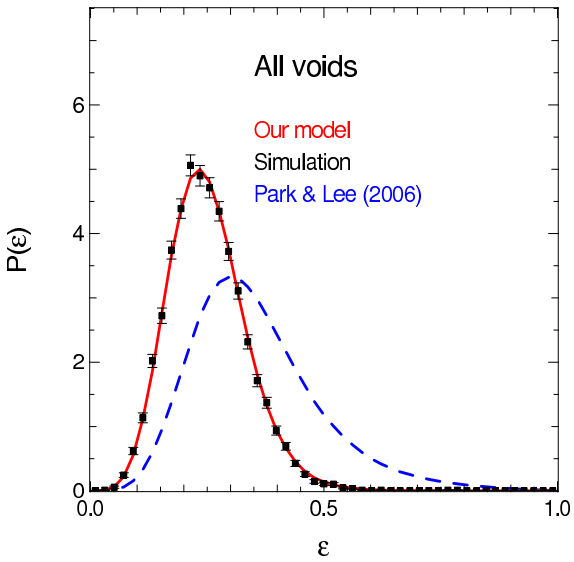

Figure 4.6: **Ellipticity distribution in voids** calculated analytically and measured in a simulation. The other curve is the theoretical distribution in the whole space as calculated by Park and Lee (2007). Figure from Lavaux and Wandelt (2010)

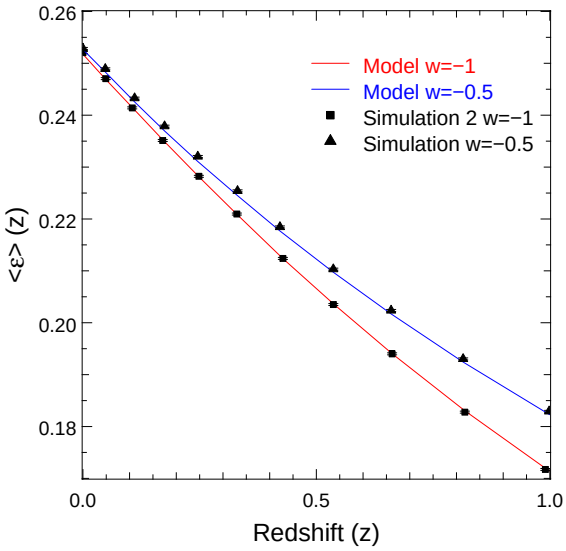

Figure 4.7: **Evolution of ellipticity** for two dark energy models. Figure from Lavaux and Wandelt (2010)

The fraction on the right side is a correction term for using Equation (4.2.6) to calculate the probability for ellipticities. We integrated over $[\nu, 1]$ because from $\lambda_2 \geq \lambda_3$ follows $\mu \geq \nu$ and from $\lambda_1 \geq \lambda_2$ that $\mu \leq 1$. Such probability curves, constructed by Park and Lee (2007) and Lavaux and Wandelt (2010), are shown in Figure 4.6.

The above shows how to calculate the ellipticity distribution of voids, but not how this distribution is changing with time. This is hidden in the seemingly unimportant parameter σ_{R_L}, the root-mean-square fluctuation of the matter density field smoothed in Lagrangian coordinates on a scale of R_L. This parameter depends explicitly on the redshift z:

$$\sigma^2_{R_L}(z) = D(z)^2 \int_{-\infty}^{\infty} \Delta(k)^2 W(kR_L)^2 d\ln k, \tag{4.2.12}$$

where $D(z)$ is the linear growth factor of the universe, $\Delta(k)$ is the power spectrum and $W(kR_L)$ is a top-hat filter for smoothing. How the growth factor $D(z)$ changes with redshift depends on the dark energy model through the evolution of its Hubble parameter:

$$D(z) = \frac{5\Omega_{m,0}H_0^2}{2} H(z) \int_z^{\infty} \frac{1+z'}{H(z')^3} dz'. \tag{4.2.13}$$

Lavaux and Wandelt (2010) investigated how the evolution of the mean ellipticities of voids depends on the equation of state of dark energy (see Figure 4.7).

Chapter 5

MAK implementations and applications

In this chapter some initial tests and analyses of MAK reconstructions will be presented, before moving on to the void shape analysis in Chapter 6. This will give some more insights into the workings of the MAK reconstruction and how inaccuracies present themselves.

5.1 2D reconstruction

To get a feeling of what the algorithm does exactly, we start by showing the result of a MAK reconstruction in two dimensions. We took a slice from an N-body simulation and only used the x- and y-coordinates. 100^2 (final) particles were randomly selected and then matched to a regular grid of 100×100 initial particles with a reconstruction. The code for the reconstruction was provided by Lavaux and Wandelt (2010)[1], and was modified for our needs. The algorithm only calculates what particles started at what initial positions. It does not consider how a particle moved from that initial position to its final position. Therefore the lines drawn in Figure 5.1 are straight lines connecting the initial and final position of a particle. Together, all the straight lines together seem to be curved along filaments on their way to the clusters. They have a pattern much like the trajectories one might find in a simulation using the adhesion approximation. This is not so surprising when we recall from Chapter 3 that a MAK reconstruction shares some properties with the adhesion approximation.

5.2 3D reconstruction

The next step was making a three-dimensional reconstruction. We used a 128^3 N-body simulation in a $(100\,\mathrm{Mpc})^3$ periodic box for our data, provided by R. van de Weygaert. Making a full reconstruction would take several weeks on a single multi-core machine, so we

[1] It can be obtained from `http://www.iap.fr/users/lavaux/code.php`

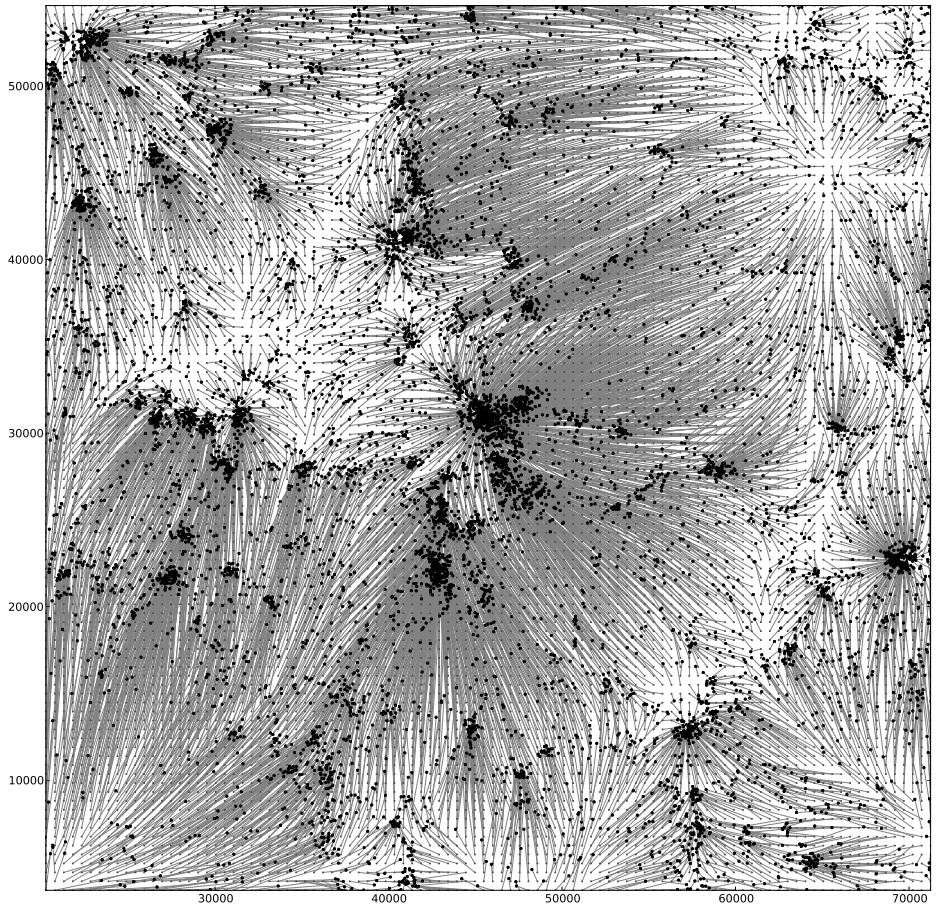

Figure 5.1: **A two-dimensional MAK reconstruction**, to illustrate what the algorithm does.

took a subset of 64^3 particles for this reconstruction. To be able to compare our reconstruction to the simulated data, we used the particle IDs to select the particles that formed a regular 64^3 grid at $t = 0$ in the simulation. A slice of the distribution and density of these 64^3 dark matter particles is displayed in Figure 5.2. The slice is centered on the largest cluster in the simulation. Now the algorithm had to connect these gridded positions to their final positions in the most optimal way. The result of the reconstruction is displayed for the same slice in Figure 5.3. We compared the reconstructed positions to the final positions in the simulation. The accuracy of the MAK reconstruction is measured by the distance between the simulated and the reconstructed final position of a certain grid particle. The connecting lines in Figure 5.3 are the reconstructed displacements, colour-coded to show the error of the reconstruction. The bottom panel of this figure highlights the inaccuracies in the reconstruction: it only shows the lines with an error in excess of 5 Mpc. As expected, the highest inaccuracies occur in high density regions.

Figure 5.4 was made to gain a better understanding of what deviations occur in the reconstruction. For each particle in the simulation, we plot its final position in the simulation ($\mathbf{x}_{sim}$) against its final position as reconstructed by MAK ($\mathbf{x}_{MAK}$). The distribution of errors in the

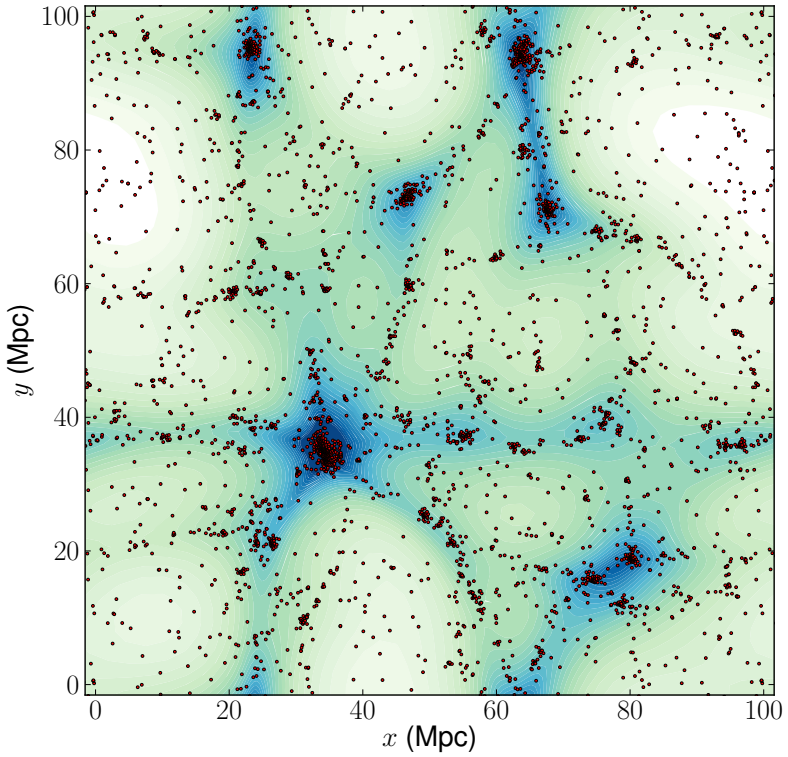

Figure 5.2: **The density field of the test simulation.** The density was derived from the dark matter distribution that is represented by the red dots. It was estimated with MAK according to Equation (6.2.7) with a Lagrangian smoothing scale of 5 Mpc.

reconstruction $\Delta\mathbf{x} = |\mathbf{x}_{MAK} - \mathbf{x}_{sim}|$ for the whole box is displayed in the inset in this figure (this quantity is also used for the colors in Figure 5.3). Two zoom-ins are displayed above the graph, showing the region inside the green boxes. It is obvious that the reconstruction is least successfull in high density regions. This is expected, because the evolution is highly non-linear in these regions. Remarkable are the cross-like patterns appearing around high density regions. This emerges because we are comparing the same set of particle positions. Take for example the large cluster in the left zoombox. Apparently, the MAK reconstruction failed to assign a significant amount of particles to the cluster from the region above it. This is the horizontal tail emanating from the cluster. These particles, that were not assigned to the cluster, had to be replaced by other particles from below the cluster, resulting in the vertical tail below it.

In a reconstruction where particles from the wrong area are assigned to a high density region, this error may propagate to other regions. The particles above the cluster that were not assigned to it have to divert to the region above. The particles that were supposed to be in this region again have to go somewhere else. This may explain why most points are below the red line in the right zoombox. However, this region is by no means representative for the whole simulation. In some regions a similar propagation may be observed, but in most cases the points are spread evenly around the line of perfect reconstruction.

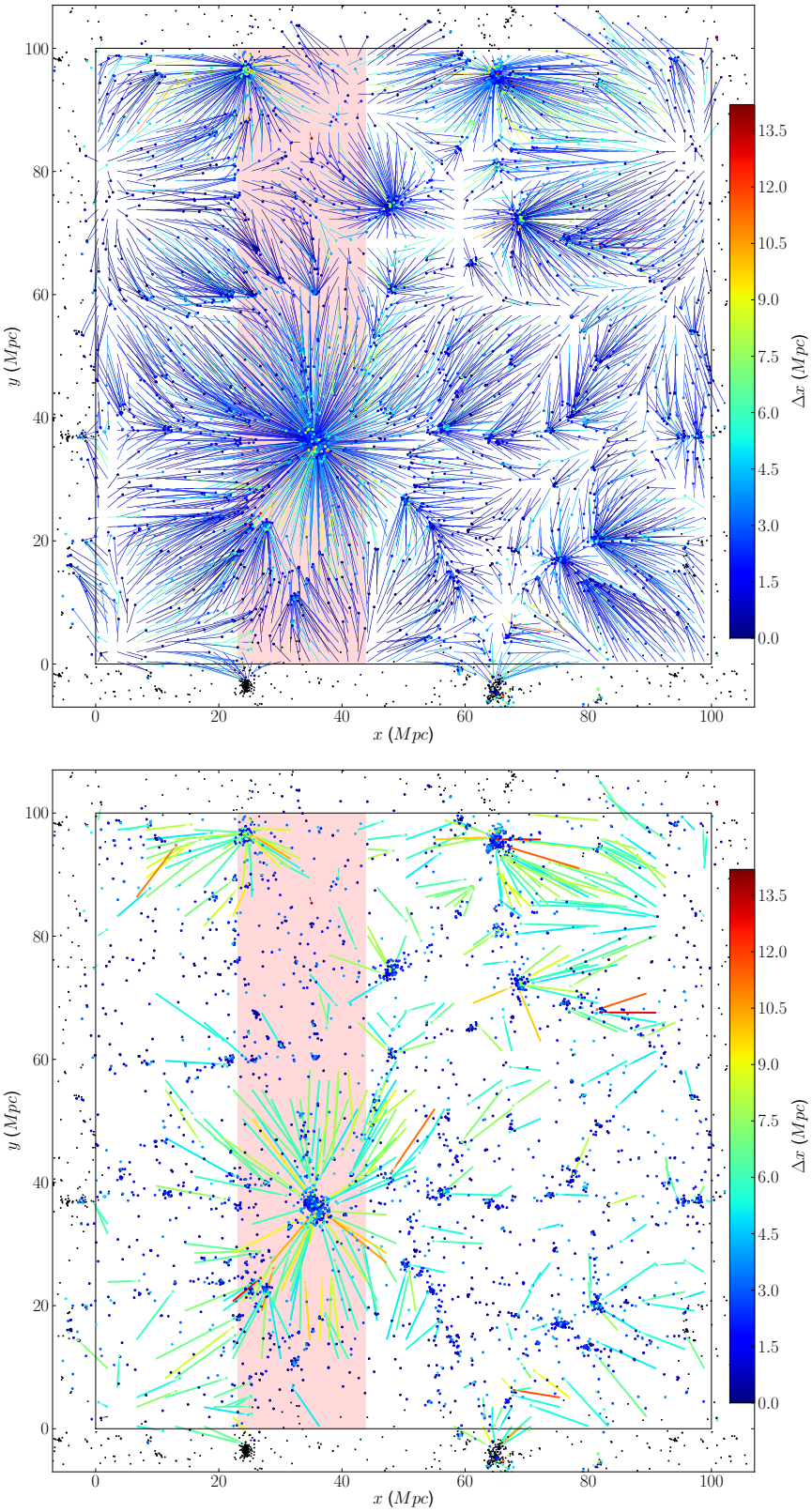

Figure 5.3: **The MAK reconstruction of the test simulation.** The colors of the lines indicate the error of the reconstruction measured by $\Delta\mathbf{x} = |\mathbf{x}_{MAK} - \mathbf{x}_{sim}|$. The vertical red highlight indicates the points that are used in Figure 5.4.

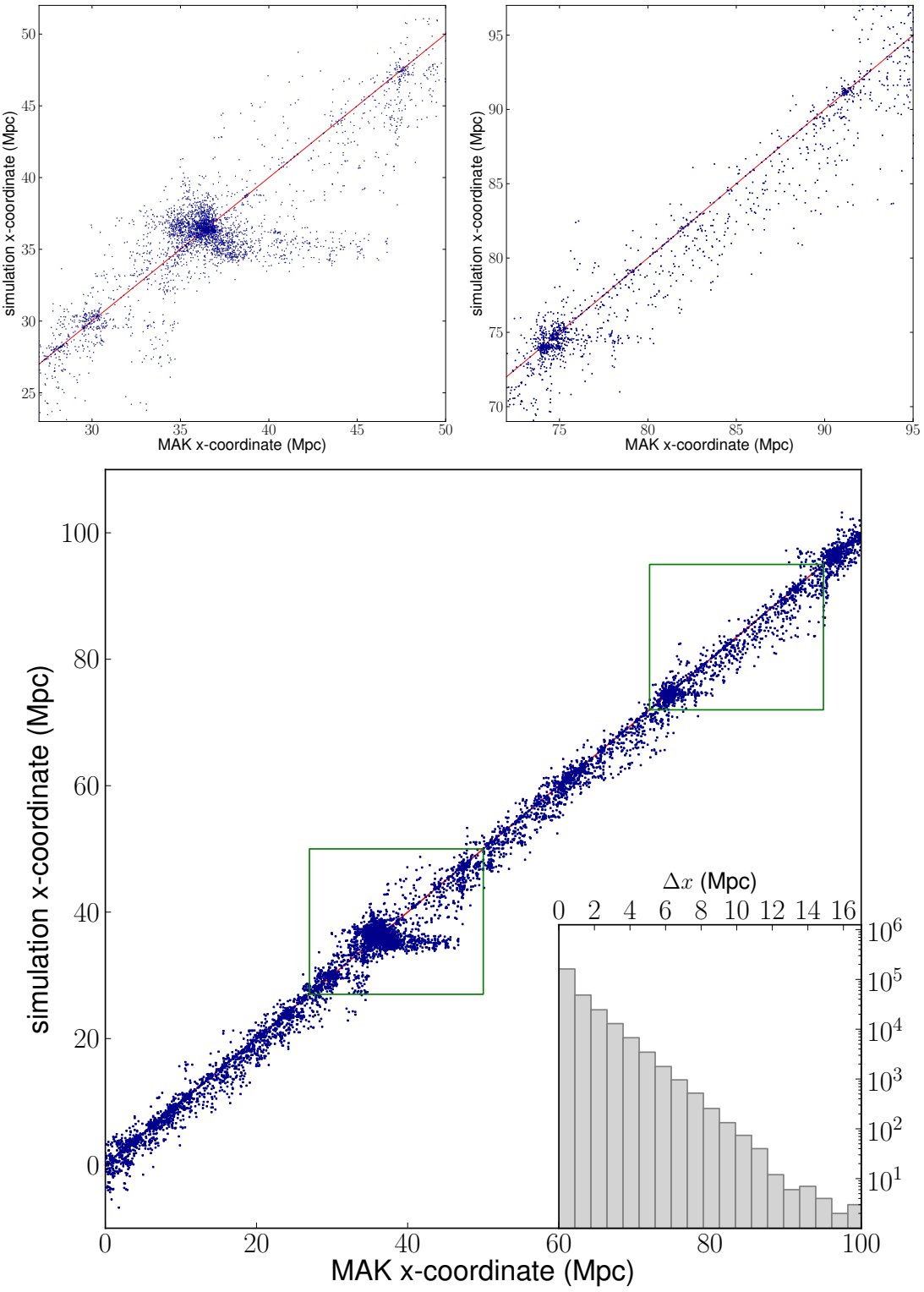

Figure 5.4: **Performance of the MAK-reconstruction.** The final positions as reconstructed by MAK are compared to the actual positions from the simulation. The red line is a one-to-one correspondence. The plotted points are from a 20 Mpc wide bar going vertically through the largest cluster, shown as a red bar in Figure 5.3. The upper panels are zoom-ins on the green boxes in the lower one. It is clear that performance is worst in high density regions. The inset shows a logarithmic histogram of the deviation from exact reconstruction $\Delta\mathbf{x} = |\mathbf{x}_{MAK} - \mathbf{x}_{sim}|$.

Chapter 6

Voids in dark energy models

As mentioned before, one of the goals of this project is to use the information obtained from a reconstruction to analyse void shapes. To this end, we used N-body simulations of several dark energy models provided by de Boni et al. (2011). The dark energy models are expected to influence the shapes of voids, the result from a study by Lavaux and Wandelt (2010) (see Section 4.2). In addition to the dark matter particle information from these simulations, we also have information on dark matter haloes. The dark matter data and the halo positions and masses extracted from the simulations were kindly provided to us by Bos (2010). The halo information can be useful as a test case for observational data, because haloes are one step in between the dark matter distribution and actual galaxies.

6.1 Simulations

The simulations were done by de Boni et al. (2011), using the `GADGET3` code, in a box containing 786^3 dark matter particles with a mass of $3.7{\cdot}10^9\, M_\odot h^{-1}$. The box has a sidelength of 300 Mpc h^{-1} on all sides, and has periodic boundary conditions. The cosmology of the simulated universe was based on the results in the third data release of the WMAP project. The initial conditions were normalized such that the σ_8 value matches that of the CMB, with a correction for the linear growth factor $D(z)$ of the specific model at the time of recombination (see Table 2.1). The simulations incorporate baryonic as well as dark matter. For the baryonic matter it includes radiative cooling and heating, star formation and the consequent feedback from winds and supernovae. The cosmological parameters used in these simulations are $\Omega_m = 0.268,\ \Omega_b = 0.044,\ \Omega_\Lambda = 0.704,\ h = 0.704,\ n = 0.947$, where Ω_m, Ω_b and Ω_Λ are the density parameters of respectively all matter, baryonic matter and dark energy, h determines the Hubble parameter through $H_0 = h/100\, km\, s^{-1}\, Mpc^{-1}$, and n the index of the primordial power spectrum. Ω_Λ is only used in the ΛCDM model, since the others do not use a cosmological constant for the dark energy.

6.1.1 Haloes

Dark matter haloes were extracted from the simulations with the `SUBFIND` algorithm (Springel et al., 2001). `SUBFIND` first uses the Friends-of-Friends (FoF) method to select high

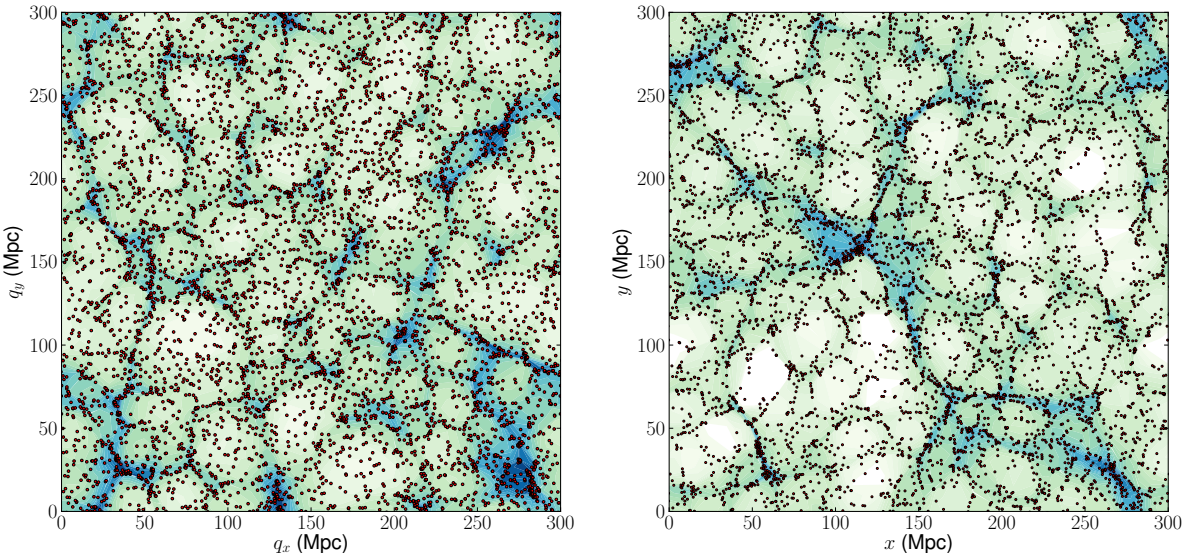

(a) Dark matter (b) Haloes

Figure 6.1: **The particle distribution and densities in the dark matter and the halo data.** Both panels show the ΛCDM model at $z = 0$. The haloes, plotted in the right panel, were derived from the dark matter distribution shown in the left panel. The density contours were determined with MAK according to Equation (6.2.7) with a Lagrangian smoothing scale of 5 Mpc. All haloes were given equal masses in the calculation, reducing the density contrast in overdense regions significantly. Note that the voids are emptier when measured with haloes, because bound structures are hard to form in an underdense expanding environment.

density areas. A FoF region is build by starting with a certain particle, and adding all its neighbours within a specific distance to its group. The group is extended further by applying the same rules to new group members iteratively. The FoF method is very efficient for finding groups of higher densities, but it usually doesn't match very well to physical entities. To find haloes that do look like physical entities like galaxies, `SUBFIND` searches within FoF groups for gravitationally bound structures. It selects candidates for haloes by constructing groups around local density maxima. It iterates over all particles sorted by background density. The particles located at local maxima become halo centers. Particles that have a neighbour with a higher density than itself will join the group of that neighbour (because of the sorting, that neighbour has already been assigned). If two of its neighbours have a higher density, but are not in the same group, the groups of the neighbours are merged. Once the candidates have been selected by following this procedure, the algorithm checks for each group which particles are gravitationally bound. All non-bound particles are discarded from the group. If the rest is still bound, they form a new halo. The halo distribution is displayed in Figure 6.1 along with the dark matter distribution from which it was derived.

Even though this algorithm retrieves both halo positions and halo masses, the latter were not used in this project. This has two reasons. Firstly, we want to use haloes because they represent galaxy-like structures. In their analysis of the dark energy simulations, de Boni et al. (2011) included a comparison of the hydrodynamics in the haloes to observed galaxies. They found good agreement in the relation between the simulated X-ray luminosity and

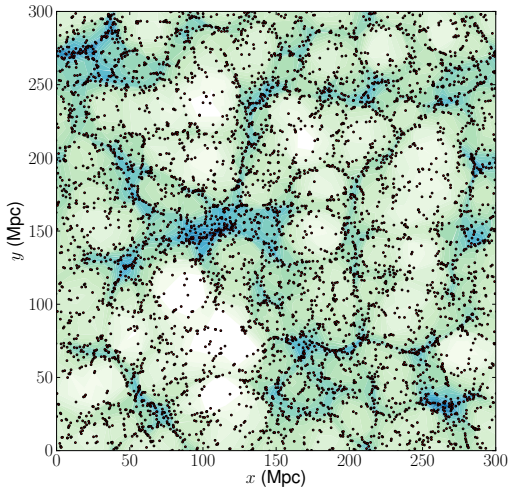

(a) $z = 1$

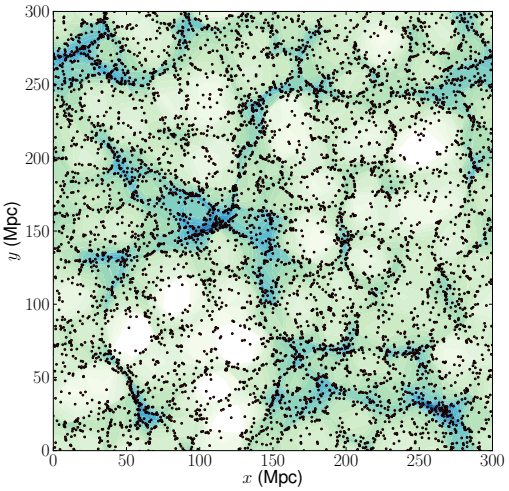

(b) $z = 0.5$

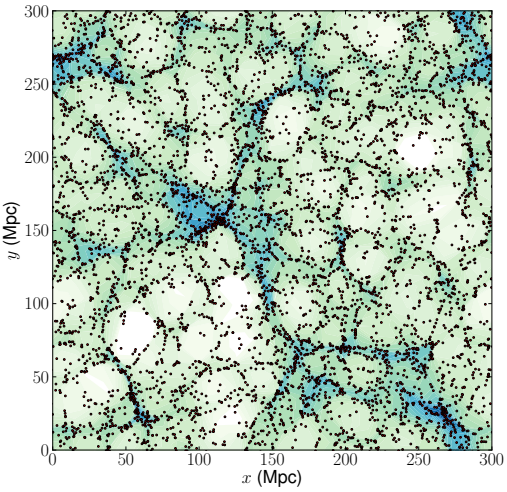

(c) $z = 0.25$

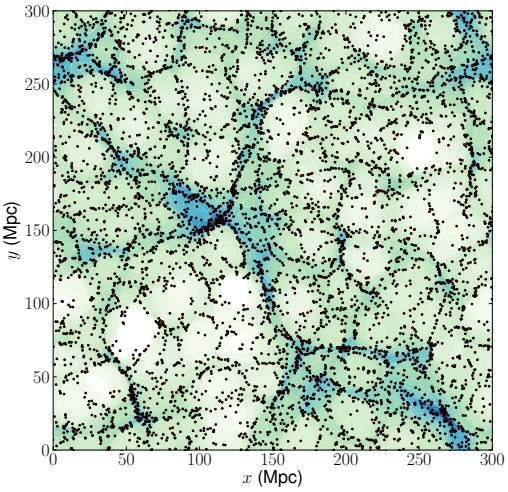

(d) $z = 0.1$

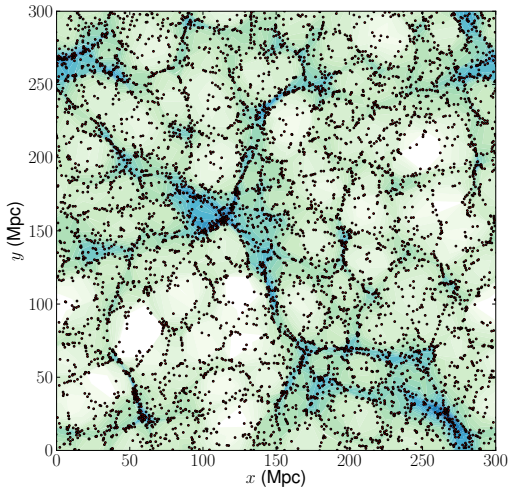

(e) $z = 0$

Figure 6.2: **Evolution of the ΛCDM model.** Plotted for each time step are the positions of the haloes in a 3.7 Mpc slice and the associated density fields determined with MAK according to Equation (6.2.7) with a Lagrangian smoothing scale of 5 Mpc. Inspecting the halo positions, the strongest evolution is visible in the first timestep, which gradually reduces to almost no visible evolution in the last timestep.

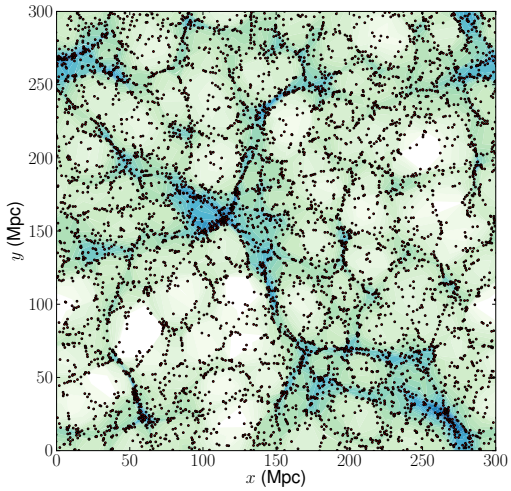

(a) ΛCDM

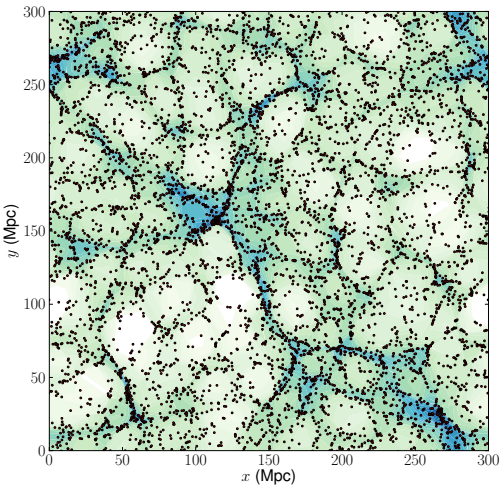

(b) EQp

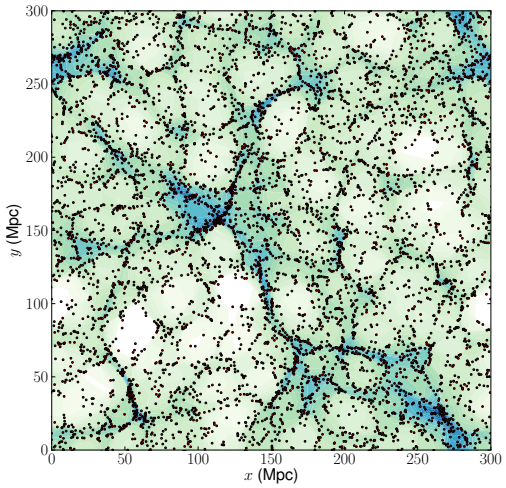

(c) RP

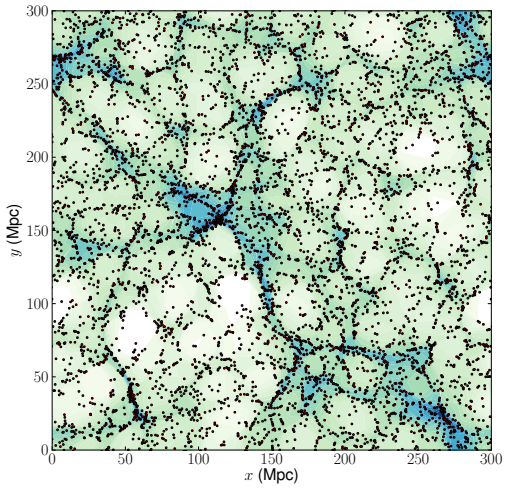

(d) EQn

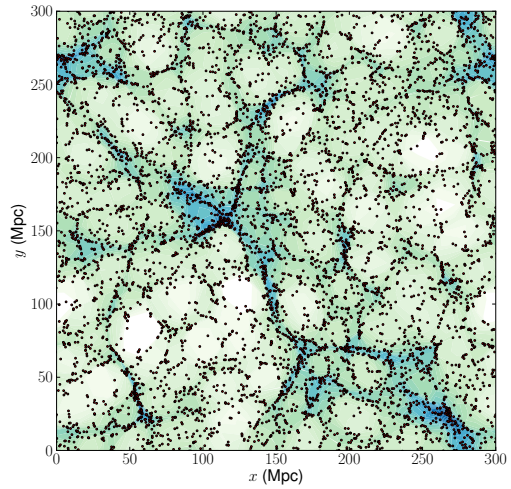

(e) SUGRA

Figure 6.3: **Density fields at $z = 0$ for all five models.** Plotted for each model are the positions of the haloes in a 3.7 Mpc slice and the associated density fields determined with MAK according to Equation (6.2.7) with a Lagrangian smoothing scale of 5 Mpc.. Although the models have diverged the most from each other at $z = 0$, hardly any difference between the models can be found by visual inspection of these slices. We will have to rely on a statistical analysis to find differences in their evolution.

the temperature compared to the observerd relation. By using the haloes extracted from a simulation and comparing the results to the dark matter data, we can see how well galaxies follow the same trends as the dark matter distribution. This way we can find out how to interpret result from observations of galaxies. Since the mass of a galaxy is hard to determine, we would prefer to use only the positions. Therefore, we leave out the masses and only use the positions of haloes in our comparison. Another reason for this is that, although in theory the displacement of particles of variable mass could be reconstructed, the Auction algorithm can only deal with uniform masses as it requires a one-to-one mapping of discrete particles.

The effect of using equally massive haloes is obvious when we compare the densities from the halo data to the dark matter density. In Figure 6.1 we see that clusters in the dark matter sample have a much higher mass concentration than in the halo sample. This can be expected since the haloes found in galaxy clusters are much more massive than haloes in the field. By neglecting this mass difference we diminish the overdensities in our halo reconstruction. In numbers, the largest cluster visible in this image has an overdensity that is thirty times larger in the dark matter distribution than it is in the haloes, calculated with Equation (6.2.7).

6.2 Analysis

From our reconstruction we obtain sets of matched initial positions $\mathbf{q}$ and final positions $\mathbf{x}$. These are first used to calculate the displacement field $\mathbf{\Psi}$

$$\mathbf{\Psi}(\mathbf{q}) = \mathbf{x}(\mathbf{q}) - \mathbf{q} \tag{6.2.1}$$

This displacement field is not used directly, but first a Lagrangian smoothing with a Gaussian kernel is applied. This is done by taking the Fourier transform of the displacement field,

$$\hat{\mathbf{\Psi}}(\mathbf{k}) = \frac{1}{(2\pi)^{1.5}} \int \mathbf{\Psi}(\mathbf{q})\, e^{i\mathbf{kq}}\, d\mathbf{q}, \tag{6.2.2}$$

and then applying the Gaussian smoothing kernel in Fourier space before transforming back:

$$\mathbf{\Psi}(\mathbf{q}) = \frac{1}{(2\pi)^{1.5}} \int \hat{\mathbf{\Psi}}(\mathbf{k})\, e^{-\frac{1}{2}\mathbf{k}^2R^2}\, e^{i\mathbf{kq}}\, d\mathbf{k}, \tag{6.2.3}$$

Here R is the smoothing scale, which we set to 5 Mpc. After smoothing we calculate the tidal shear tensor as:

$$\mathbf{T}_{i,j}(\mathbf{q}) = \frac{\partial \mathbf{\Psi_i}(\mathbf{q})}{\partial \mathbf{q}_j} = \frac{\partial^2 \Phi(\mathbf{q})}{\partial \mathbf{q}_i \partial \mathbf{q}_j} \tag{6.2.4}$$

This derivative of the displacement field is calculated in Fourier space:

$$\frac{\partial \mathbf{\Psi}(\mathbf{q})}{\partial \mathbf{q}} = \frac{\partial}{\partial \mathbf{q}} \frac{1}{(2\pi)^{1.5}} \int \hat{\mathbf{\Psi}}(\mathbf{k})\, e^{-\frac{1}{2}\mathbf{k}^2R^2}\, e^{i\mathbf{kq}}\, d\mathbf{k} = \frac{1}{(2\pi)^{1.5}} \int i\mathbf{k}\hat{\mathbf{\Psi}}(\mathbf{k})\, e^{-2\pi i\mathbf{kq}}\, d\mathbf{k} \tag{6.2.5}$$

Then we calculate the eigenvalues of the tidal shear tensor and sort them in descending order. These eigenvalues (λ_i) can be used for the shape analysis described in Section 4.2.

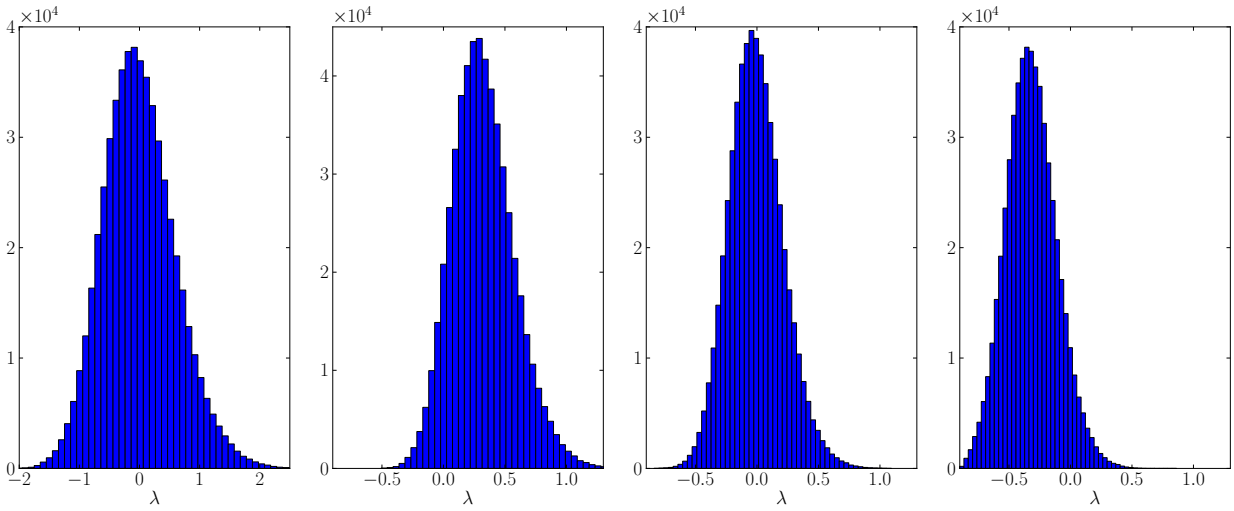

(a) $\sum \lambda_i$ (b) λ_1 (c) λ_2 (d) λ_3

Figure 6.4: **The distribution of λ values** in the reconstruction of haloes in the ΛCDM model at $z = 0$. The shape of the distributions is rather similar for other models and other times: there is only a small systematic decrease (of ~ 0.2) in the eigenvalues from $z = 1$ to $z = 0$. Since the values are sorted in descending order, the distribution shifts towards negative numbers from λ_1 to λ_3. The far left panel shows the distribution of the sum of the eigenvalues. This is an approximation for the local underdensity.

Figure 6.5: **An ellipse with ellipticity $\varepsilon = 0.29$.** A unit sphere has major and minor axis lengths $a = 1$ and $c = 1$. When this sphere is stretched by a tidal shear tensor with eigenvalues $\lambda_1 = 1$ and $\lambda_3 = 0$, its axis lengths become $a = 2$ and $c = 1$ which corresponds to an ellipticity of $\varepsilon = 0.29$. The eigenvalue λ_2 affects the semi-major axis, which is irrelevant for the ellipticity calculation.

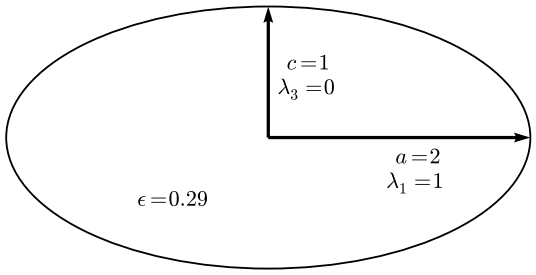

The distributions of the eigenvalues and their sum can be inspected in Figure 6.4. The ellipticity parameter is:

$$\varepsilon = 1 - \sqrt{\frac{1+\lambda_3}{1+\lambda_1}} \tag{6.2.6}$$

An ellipse with a typical void ellipticity of $\varepsilon = 0.29$ is illustrated is Figure 6.5. Its major axis length is $a = 1 + \lambda_1$ and the minor axis length is $c = 1 + \lambda_3$. The density at a point $\mathbf{q}$ corresponding to these eigenvalues is:

$$\rho(\mathbf{q}) = \rho_0(\mathbf{q})\,|J_{i,j}| = \frac{\rho_0(\mathbf{q})}{(\lambda_1+1)(\lambda_2+1)(\lambda_3+1)} \tag{6.2.7}$$

This equation has been used to calculate the densities displayed in Figures 6.1, 6.2 and 6.3. In Figure 6.2 we clearly see that the density contrast is lower in the earlier stage of the evolution of ΛCDM. The ΛCDM shows the strongest evolution of all models. In Figure 6.3 we show

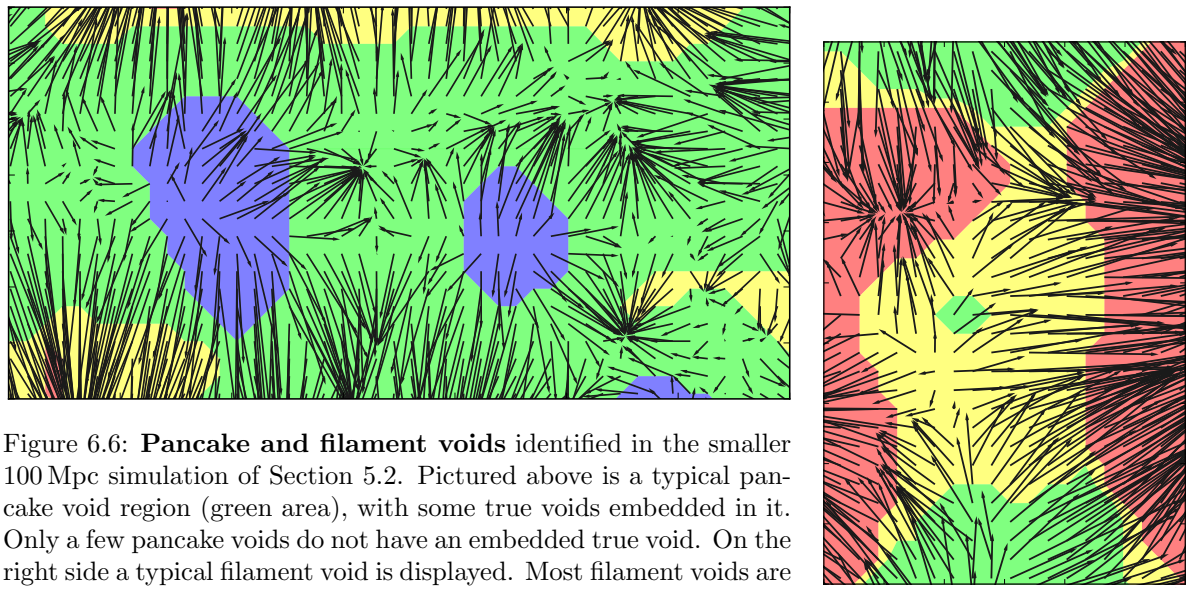

Figure 6.6: **Pancake and filament voids** identified in the smaller 100 Mpc simulation of Section 5.2. Pictured above is a typical pancake void region (green area), with some true voids embedded in it. Only a few pancake voids do not have an embedded true void. On the right side a typical filament void is displayed. Most filament voids are between two clusters or completely surrounded by overdense regions.

the haloes and densities in all models at $z = 0$. As expected, the overdensities in this model are not quite as high as in the ΛCDM model at $z = 0$.

6.3 Void ellipticity

6.3.1 Dynamical types

Because we want to study all voids, we must distinguish between three dynamical types. We define a *filament void* as an underdense region with only one positive eigenvalue, i.e. a region expanding in one direction. A *pancake void* expands in two directions, while for a *true void* all eigenvalues have to be positive. We need an additional constraint to restrict ourselves to underdense regions, otherwise walls and filaments may be included. We use the sum of the eigenvalues as an approximation for the (under)density[1], and require $\sum \lambda_i > 0$ for all void-like regions. The distributions of the eigenvalues and their sum can be inspected in Figure 6.4. In this project we will mostly discuss the collection of all three void types, which will be referred to as '*all voids*'. Our selection criteria for this collection are $\lambda_1 > 0$ and $\sum \lambda_i > 0$. In the distribution we see that $\lambda_1 > 0$ nearly everywhere, so we can conclude from the distribution of $\sum \lambda_i$ (Fig. 6.4a) that approximately half of our Lagrangian volume is included in the *all voids* selection. However, Figure 6.4d tells us that only a very small fraction of our data may be classified as a *true void*. This is a major disadvantage when we want to study the statistical properties in these regions. For this reason most of our analysis will be done using *all voids*.

[1]This approximation can be verified by doing a Taylor expansion of Equation (6.2.7) for the local density to the first order.

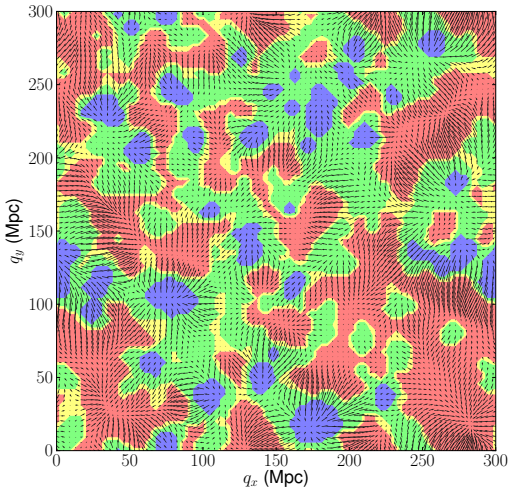

(a) ΛCDM

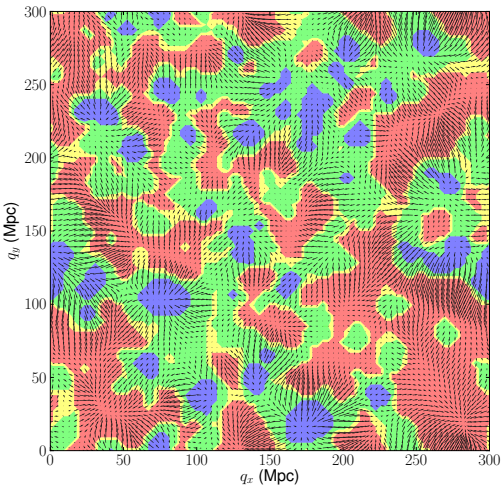

(b) EQp

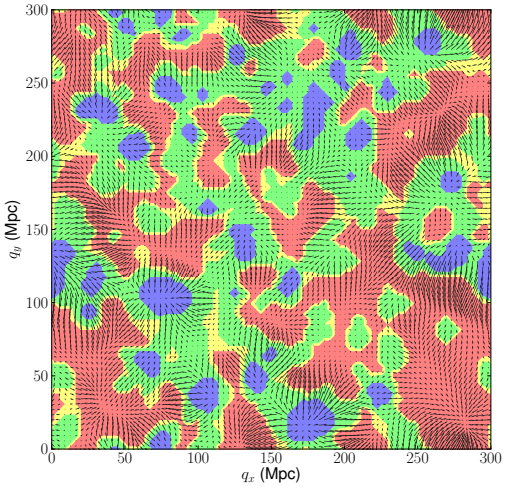

(c) RP

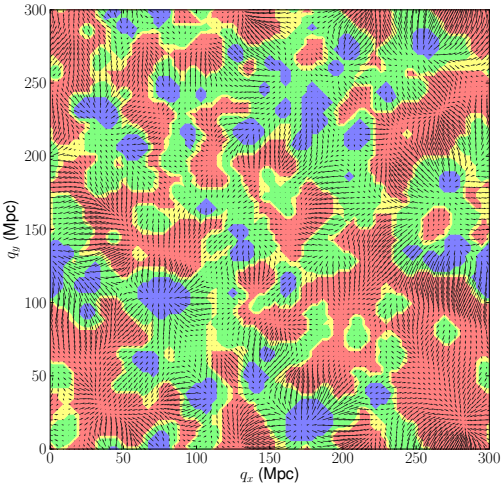

(d) EQn

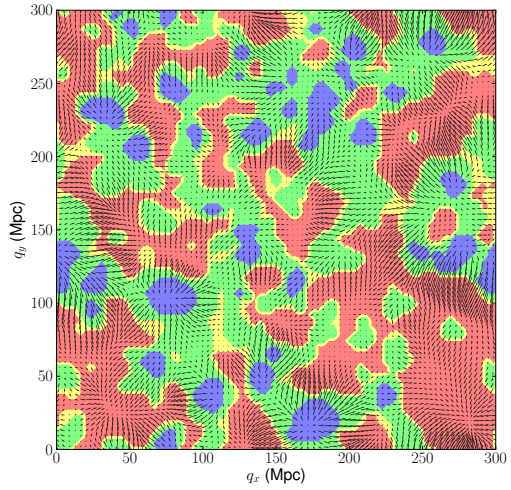

(e) SUGRA

Figure 6.7: **Void types at $z = 0$.** The types are derived from the reconstruction of haloes and are displayed as a 3.7 Mpc thick slice, i.e. one grid cell width, in Lagrangian space. In the image, blue regions are *true voids* which are usually surrounded by green *pancake voids*. The *filament voids*, highlighted in yellow, are usually found as thin layers around *pancake voids*, although sometimes they actually filament-like structeres that become underdense due to strong tidal forces inside a large void or in between high density structures. Red shaded areas are overdense regions and are not included in this study.

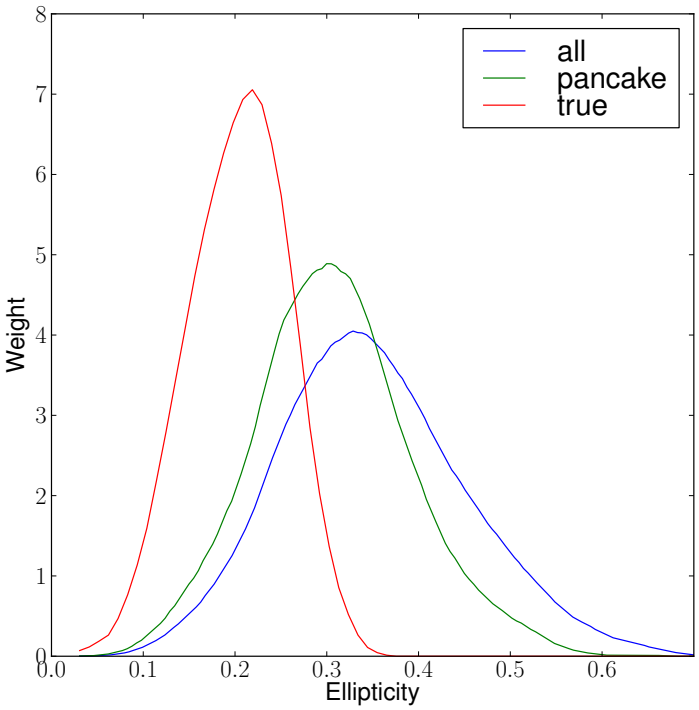

Figure 6.8: **Ellipticity distributions for the different types of voids.** Lavaux and Wandelt (2010) proved that *true voids* have a lower mean ellipticity with a more peaked distribution than *all voids*. We see that this is indeed true for our simulation. We also show a distribution for *pancake voids* (but also including the *true voids*). As expected, it lies between the other two distributions.

How the different void types present themselves can be inspected in Figure 6.7. It shows the Lagrangian distribution of the different types of voids in all five models at present time. In the figure, the *true voids* seem to reside in the most underdense regions and are encompassed by *pancake voids*. Together these two types occupy most of the underdense area: $\sim 6.7\%$ and $\sim 33.5\%$ of the whole Lagrangian volume respectively. These numbers only deviate below the 1% level between the models. The *filament voids* mostly form a thin border around the *pancake void* regions. They only rarely form a void themselves in between overdense areas, like the one shown in Figure 6.6. Sometimes a filament structure extending into a large void can become underdense due to the strong divergent forces in the void. Such a filament will also be classified as a *filament void*. All these different manifestations of *filament voids* only account for $\sim 7\%$ of the Lagrangian volume. The rest of the Lagrangian volume, $\sim 53\%$ is occupied by overdense regions. Because the Lagrangian coordinates represent the initial uniform distribution of haloes, the Lagrangian volume occupied by a certain structure is a measure for the number of haloes residing in it. When all particles have equal mass, it even measures the mass of the structure. However, we have not included the halo masses in this study, so the Lagrangian volumes mentioned above only represent a number of haloes.

6.3.2 Ellipticity distributions

For our next step we calculate the ellipticity in void-like regions. The ellipticity at a point $\mathbf{q}$ is:

$$\varepsilon(\mathbf{q}) = 1 - \sqrt{\frac{\lambda_3(\mathbf{q}) + 1}{\lambda_1(\mathbf{q}) + 1}}. \tag{6.3.1}$$

Now we want to inspect the distribution of ellipticities in voids. We first select the points in underdense regions where $\sum \lambda_i > 0$ and sort the list of ellipticities at these points. To plot

the probability function of the ellipticity ε for these regions, we take the derivative of the cumulative ε distribution,

$$P(\varepsilon) = \frac{n(< \varepsilon + \Delta\varepsilon) - n(< \varepsilon)}{N\,\Delta\varepsilon}. \tag{6.3.2}$$

Here $n(< \varepsilon)$ means the number of points where the ellipticity is smaller than ε, and $\Delta\varepsilon$ is the stepsize for this derivative calculation. In Figure 6.8 we show what these distributions look like for the different types of voids. This curve was derived from the 100 Mpc simulation described earlier.

Some of the probability curves for our dark energy models can be seen in Figure 6.9. The curves in the upper graphs of this figure show the evolution of the ellipticities of voids for two models. As may be expected from their equation of state, the ΛCDM model evolves noticeably faster than the SUGRA model. In the bottom graphs of this figure the ellipticities in different models at a certain time are displayed. At $z = 1$ in the left graph the distributions hardly differ. The reason is that the models were normalized at recombination. The dark energy that would cause differences in ellipticity only becomes dominant just before $z = 1$. However, in the right graph at $z = 0$, we do see significant differences between the models. At this time the dark energy has apparently had enough time to influence the ellipticities to a measurable level.

6.3.3 Void Evolution

To study the evolution of all models it is more convenient not to look at the distribution of ellipticities, but just at the mean. For each model at each timestep we took the mean of all ellipticities at the points that have $\sum \lambda_i > 0$. These mean ellipticities are plotted against the redshift of the corresponding timestep in Figure 6.10. We see that there is indeed a significant difference between the models. The first thing that stands out is that the models still lie close together at $z = 1$ because of the normalization (as we already saw in Figure 6.9c). The evolution of the ellipticity after $z = 1$ heavily depends on the equation of state of dark energy. For convenience we will show Figure 2.8 from Section 4.2 again. Looking at these two figures side-by-side it is not so hard to explain the observed ellipticity evolution. The SUGRA model, which initially has the highest value of w, shows the least change with redshift. On the other hand the ΛCDM model with the lowest value of w shows the strongest evolution. The RP, EQn and EQp models show a very close resemblance to each other in both figures. The RP and EQp models are hardly distinguishable at all in the ellipticity evolution. The EQn model is also very close to these two, but it has a slightly higher w-value at $z = 1$, which may explain why it does not evolve as much as the other two. We will have to do some more analysis to determine whether these three models are significantly different.

To be able to say something about the significance of the points in Figure 6.10 we will have to do some statistical tests. We used the jackknife method to calculate an upperbound for the errors on our values. For every point in Figure 6.10, that each represents the result of a reconstruction with $\sim 80^3$ particles, we took 8 subsets of 32^3 particles for the jackknife analysis. In addition, we did a Kolmogorov-Smirnov test (KS-test) on the cumulative ellipticity curves from which the curves in Figure 6.9 were derived. The KS-test gives the confidence level that

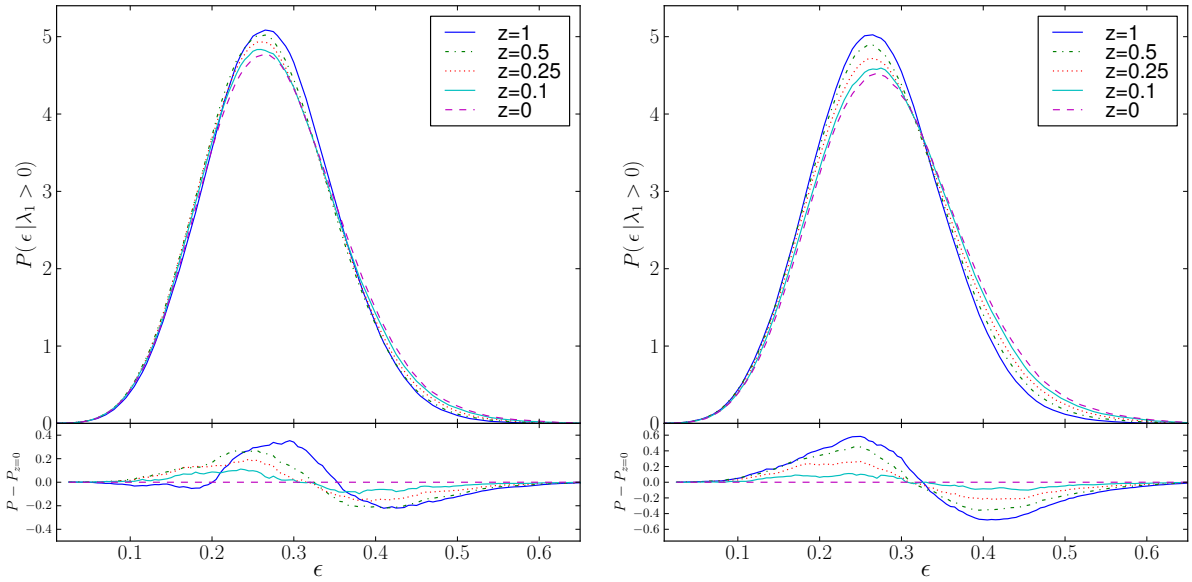

(a) **SUGRA** (b) **ΛCDM**

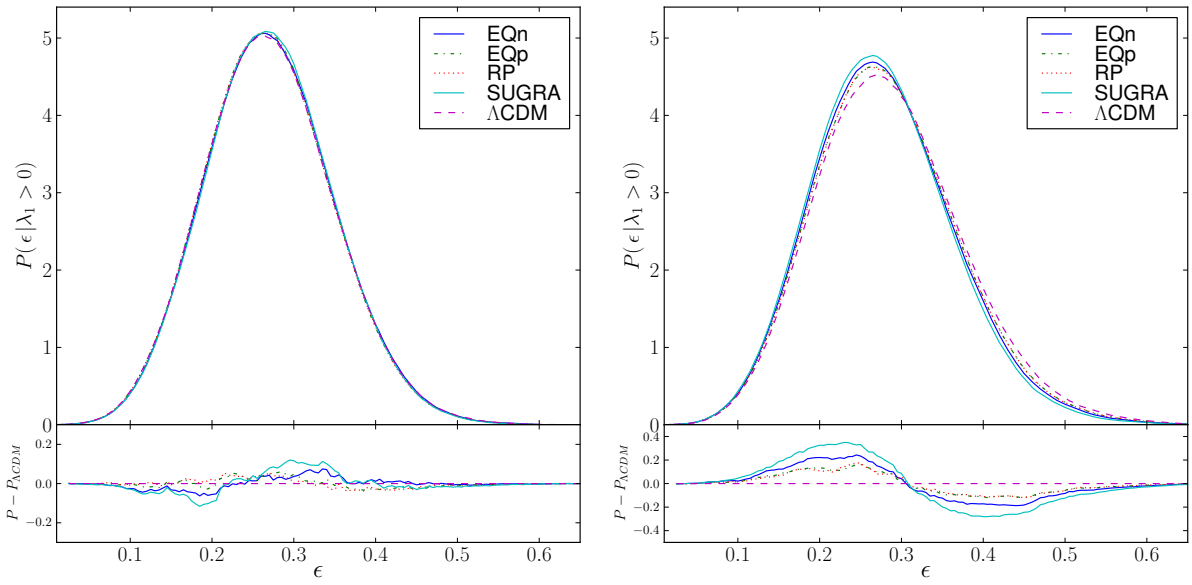

(c) $\mathbf{z = 1}$ (d) $\mathbf{z = 0}$

Figure 6.9: **Ellipticity distributions** found for *all voids* in the halo data. In the top row the evolution from $z = 1$ to $z = 0$ in the SUGRA and the ΛCDM models is displayed. It is clear that both models evolve, but the ΛCDM model on the right evolves faster than the SUGRA model on the left. The bottom row shows the state of all five models at a fixed point in time. At the early stage of $z = 1$ in the bottom left panel, the models are more or less equal. At present time $z = 0$ shown on the right, there is a clear separation between most of the models.

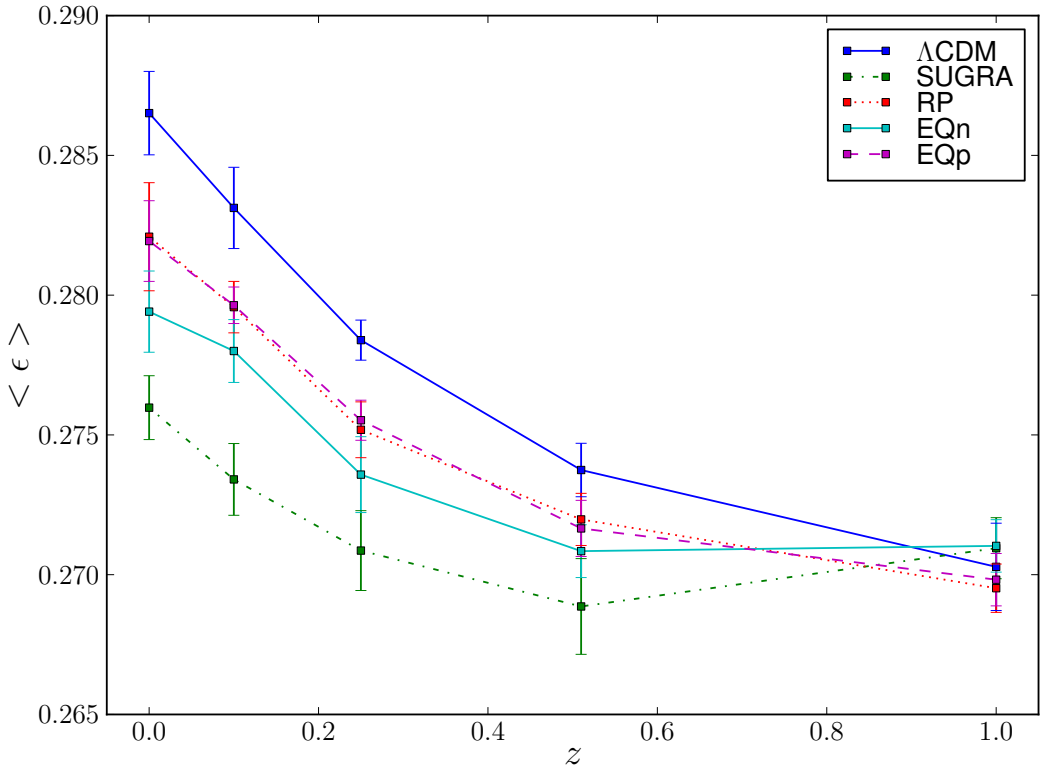

Figure 6.10: **Mean ellipticity as a function of redshift** in *all voids* in the halo samples of the five dark energy simulations.

two samples are drawn from the same distribution. The RP and EQp models could not be distinguished with a high confidence: the probability of being equal ranges from $P = .02$ at $z = 0.25$ up to $P = .99$ at $z = 0.1$. All other models at all other times (even $z = 1$) could be clearly distinguished at a confidence level of $P < 0.05$. The upperbound error estimates were not included in the calculation of the KS-statistics.

With these statistics we can claim with much more certainty that indeed the ellipticity evolutions of all dark matter models in Figure 6.10 are significantly different from each other, except for the RP and EQp models. Although none of the models are clearly separable at $z = 1$ due to the error, they diverge in their evolution towards $z = 0$ such that only the RP and EQp models are indistinguishable. When comparing these results to Figure 2.8, the big difference between the SUGRA, the ΛCDM and the other models is not surprising. The fact that the RP and EQp model are hardly distinguishable, while the EQn model is clearly separated from these two, is not explained by Figure 2.8. The equation of state parameter for the RP model is actually much closer to EQn than to EQp. However, the equation of state does not fully describe a model. Possibly modified gravity due to the coupling in the extended quintessence models has more influences on the void shape than the equation of state. An additional remarkable feature is the fact that the ellipticities of the EQn and SUGRA models seem to decrease in the first timestep. In the case of EQn this decrease is not significant within the errors, but it is for the SUGRA model. We have not found an explanation for this.

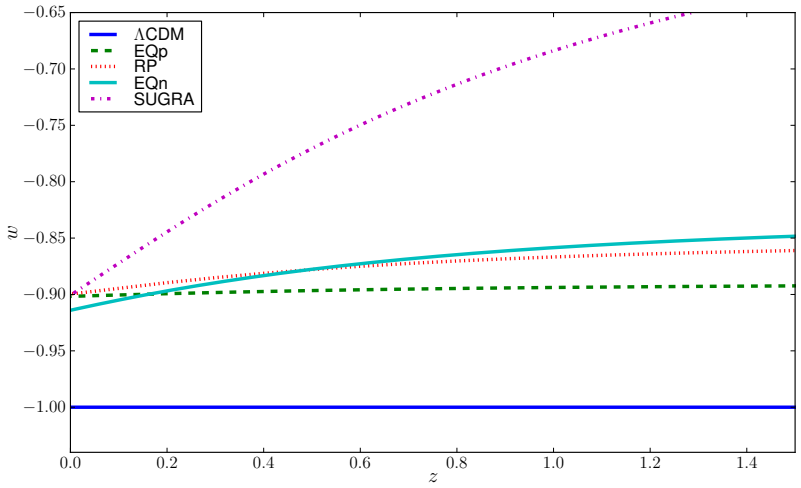

Figure 2.8: **The evolution of the w parameter for dark energy models.** This is a repeat of Figure 2.8. The equation of state parameter is defined as $w \equiv P/\rho$. Figure data from de Boni et al. (2011).

Chapter 7

Conclusions

7.1 The MAK reconstruction

The Monge-Ampère-Kantorovitch reconstruction is an excellent method for Lagrangian and dynamical studies of the large scale structure. Authors like Frisch et al. (2002) and Brenier et al. (2003) have already shown that this method can produce an accurate reconstruction of velocities of dark matter particles in a simulation. With the prospect of applying this method to large galaxy redshift surveys, they also reconstructed velocities in redshift space and got equally promising results. For the same reason, we applied the method to gravitationally bound haloes in hydrodynamical simulations. We found that the reconstruction was very accurate. It was most inaccurate in high density regions due to a slight inconvenience: there is a non-trivial problem in incorporating the masses of haloes in the reconstruction. However, this problem only affects the high density regions where the reconstruction already was the least accurate. In the rest of the volume the MAK reconstruction shows the same results for haloes as it does for dark matter.

MAK is a most promising method in those case where we cannot obtain all the dynamical information we need. It allows us to obtain an approximation of the full dynamical information, while it only requires the positions of objects as input. Since Brenier et al. (2003) have shown that the reconstruction is nearly as effective in redshift space as it is in normal coordinates, this method will be very useful in studies of large redshift surveys of the large scale structure.

7.2 Void shapes

In this project we presented an analysis of the evolution of void shapes. We showed that this evolution was different in simulations with different models for dark energy. Furthermore, the reconstruction was performed on dark matter haloes, which are somewhat representative for galaxies. This was done as a test case for applying this analysis to observed galaxy distributions, the ultimate goal for this method. We found that our results were similar to

those of Lavaux and Wandelt (2010). The ellipticity of voids increases as they evolve, and the lower the w parameter for the dark energy, the higher this increase is.

From these two findings we can conclude that this is a promising technique in our search for dark energy. We can use the MAK reconstruction method on large redshift surveys to measure void ellipticities. This will allows us to exclude certain models for dark energy based on void shapes in simulations. How tight the constraints on models from this method will be is still uncertain and will require more extensive studies.

Acknowledgements

I would like to thank Rien van de Weygaert for his thorough supervision over this project. I am very grateful to Patrick Bos for providing me with simulation data and answering all my questions about them. Thanks go to the cosmology group for the useful discussions during our meetings, and in particular to Johan for proving some insights into Lagrangian theory and for the beautiful figures he gave me. I would also like to acknowledge my fellow students for good discussion and general good times, and in particular André and Eva who completely read and commented on my report. Finally, thanks go to de Boni et al. (2011) for allowing my to use their data in this project.

Bibliography

Acquaviva, V., Baccigalupi, C., Leach, S. M., Liddle, A. R., and Perrotta, F. (2005). Structure formation constraints on the Jordan-Brans-Dicke theory. *Phys. Rev. D*, 71:104025.

Baldi, M. (2011). Clarifying the effects of interacting dark energy on linear and non-linear structure formation processes. *MNRAS*, 414:116–128.

Benamou, J.-D. and Brenier, Y. (2000). A computational fluid mechanics solution to the monge-kantorovich mass transfer problem. *Numerische Mathematik*, 84:375–393.

Bennett, C. L., Banday, A. J., Gorski, K. M., Hinshaw, G., Jackson, P., Keegstra, P., Kogut, A., Smoot, G. F., Wilkinson, D. T., and Wright, E. L. (1996). Four-Year COBE DMR Cosmic Microwave Background Observations: Maps and Basic Results. *ApJL*, 464:L1–+.

Bertotti, B., Iess, L., and Tortora, P. (2003). A test of general relativity using radio links with the Cassini spacecraft. *Nature*, 425:374–376.

Bertsekas, D. P. The Auction Algorithm for assignment and other network flow problems. *Interfaces*.

Bertsekas, D. P. (1988). The Auction Algorithm: A Distributed Relaxation Method for the Assignment Problem. *Annals of Operations Research*, 14:105–123.

Bond, J. R. (1987). Testing cosmic fluctuation spectra. In *Nearly Normal Galaxies. From the Planck Time to the Present*, pages 388–397.

Bos, E. G. P. (2010). Voids as Probes fo the Nature of Dark Energy. *MSc Thesis*.

Brans, C. and Dicke, R. H. (1961). Mach's principle and a relativistic theory of gravitation. *Phys. Rev.*, 124:925–935.

Brax, P. H. and Martin, J. (1999). Quintessence and supergravity. *Phys. Let. B*, 468:40–45.

Brenier, Y., Frisch, U., Hénon, M., Loeper, G., Matarrese, S., Mohayaee, R., and Sobolevskiĭ, A. (2003). Reconstruction of the early Universe as a convex optimization problem. *MNRAS*, 346:501–524.

Brunino, R., Trujillo, I., Pearce, F. R., and Thomas, P. A. (2007). The orientation of galaxy dark matter haloes around cosmic voids. *MNRAS*, 375:184–190.

Colberg, J. M., Pearce, F., Foster, C., Platen, E., Brunino, R., Neyrinck, M., Basilakos, S., Fairall, A., Feldman, H., Gottlöber, S., Hahn, O., Hoyle, F., Müller, V., Nelson, L., Plionis, M., Porciani, C., Shandarin, S., Vogeley, M. S., and van de Weygaert, R. (2008). The Aspen-Amsterdam void finder comparison project. *MNRAS*, 387:933–944.

Colberg, J. M., Sheth, R. K., Diaferio, A., Gao, L., and Yoshida, N. (2005). Voids in a ΛCDM universe. *MNRAS*, 360:216–226.

Colless, M., Peterson, B. A., Jackson, C., Peacock, J. A., Cole, S., Norberg, P., Baldry, I. K., Baugh, C. M., Bland-Hawthorn, J., Bridges, T., Cannon, R., Collins, C., Couch, W., Cross, N., Dalton, G., De Propris, R., Driver, S. P., Efstathiou, G., Ellis, R. S., Frenk, C. S., Glazebrook, K., Lahav, O., Lewis, I., Lumsden, S., Maddox, S., Madgwick, D., Sutherland, W., and Taylor, K. (2003). The 2dF Galaxy Redshift Survey: Final Data Release. *ArXiv Astrophysics e-prints*, astro-ph/0306581.

de Boni, C., Dolag, K., Ettori, S., Moscardini, L., Pettorino, V., and Baccigalupi, C. (2011). Hydrodynamical simulations of galaxy clusters in dark energy cosmologies - I. General properties. *MNRAS*, 415:2758–2772.

Doroshkevich, A. G. (1970). The space structure of perturbations and the origin of rotation of galaxies in the theory of fluctuation. *Astrofizika*, 6:581–600.

Faber, S. M. and Gallagher, J. S. (1979). Masses and mass-to-light ratios of galaxies. *An. Rev. of A&A*, 17:135–187.

Frisch, U., Matarrese, S., Mohayaee, R., and Sobolevskiĭ, A. (2002). A reconstruction of the initial conditions of the Universe by optimal mass transportation. *Nature*, 417:260–262.

Gottlöber, S., Łokas, E. L., Klypin, A., and Hoffman, Y. (2003). The structure of voids. *MNRAS*, 344:715–724.

Gregory, S. A. and Thompson, L. A. (1978). The Coma/A1367 supercluster and its environs. *ApJ*, 222:784–799.

Gurbatov, S. N. and Saichev, A. I. (1984). Probability distribution and spectra of potential hydrodynamic turbulence. *Radiophysics and Quantum Electronics*, 27:303–313.

Hahn, O., Porciani, C., Carollo, C. M., and Dekel, A. (2007). Properties of dark matter haloes in clusters, filaments, sheets and voids. *MNRAS*, 375:489–499.

Heath, D. J. (1977). The growth of density perturbations in zero pressure Friedmann-Lemaître universes. *MNRAS*, 179:351–358.

Hicken, M., Wood-Vasey, W. M., Blondin, S., Challis, P., Jha, S., Kelly, P. L., Rest, A., and Kirshner, R. P. (2009). Improved Dark Energy Constraints from ˜100 New CfA Supernova Type Ia Light Curves. *ApJ*, 700:1097–1140.

Hidding, J., van de Weygaert, R., Vegter, G., and Jones, B. J. T. (2011). Cosmic Voids: structure, dynamics and galaxies. *MNRAS*, to be subm.

Hoyle, F. and Vogeley, M. S. (2002). Voids in the Point Source Catalogue Survey and the Updated Zwicky Catalog. *ApJ*, 566:641–651.

Joeveer, M., Einasto, J., and Tago, E. (1978). Spatial distribution of galaxies and of clusters of galaxies in the southern galactic hemisphere. *MNRAS*, 185:357–370.

Kantorovich, L. V. *Proceedings of the USSR Academy of Sciences*, 37:227.

Komatsu, E., Smith, K. M., Dunkley, J., Bennett, C. L., Gold, B., Hinshaw, G., Jarosik, N., Larson, D., Nolta, M. R., Page, L., Spergel, D. N., Halpern, M., Hill, R. S., Kogut, A., Limon, M., Meyer, S. S., Odegard, N., Tucker, G. S., Weiland, J. L., Wollack, E., and Wright, E. L. (2011). Seven-year Wilkinson Microwave Anisotropy Probe (WMAP) Observations: Cosmological Interpretation. *ApJS*, 192:18–+.

Lavaux, G. (2010). Dynamics of the Local Universe: cosmic velocity flows and voids. In *American Institute of Physics Conference Series*, volume 1241, pages 1001–1010.

Lavaux, G. and Wandelt, B. D. (2010). Precision cosmology with voids: definition, methods, dynamics. *MNRAS*, 403:1392–1408.

Lee, J. and Park, D. (2009). Constraining the Dark Energy Equation of State with Cosmic Voids. *ApJ*, 696:L10–L12.

Lyth, D. H. and Riotto, A. (1999). Particle physics models of inflation and the cosmological density perturbation. *Phys. Rep.*, 314:1–146.

Mohayaee, R. and Tully, R. B. (2005). The Cosmological Mean Density and Its Local Variations Probed by Peculiar Velocities. *ApJL*, 635:L113–L116.

Monge, G. (1781). Sur la théorie des déblais et des remblais. *Histoire de l'académie des Sciences de Paris*, pages 666–704.

Müller, V., Arbabi-Bidgoli, S., Einasto, J., and Tucker, D. (2000). Voids in the Las Campanas Redshift Survey versus cold dark matter models. *MNRAS*, 318:280–288.

Nusser, A. and Dekel, A. (1992). Tracing large-scale fluctuations back in time. *ApJ*, 391:443–452.

Park, D. and Lee, J. (2007). Void Ellipticity Distribution as a Probe of Cosmology. *Phys. Rev. Let.*, 98:081301.

Peebles, P. J. E. (1989). Tracing galaxy orbits back in time. *ApJL*, 344:L53–L56.

Peebles, P. J. E. and Ratra, B. (1988). Cosmology with a time-variable cosmological 'constant'. *ApJ*, 325:L17–L20.

Pettorino, V. and Baccigalupi, C. (2008). Coupled and extended quintessence: Theoretical differences and structure formation. *Phys. Rev. D*, 77:103003.

Platen, E., van de Weygaert, R., and Jones, B. J. T. (2007). A cosmic watershed: the WVF void detection technique. *MNRAS*, 380:551–570.

Riess, A. G., Filippenko, A. V., Challis, P., Clocchiatti, A., Diercks, A., Garnavich, P. M., Gilliland, R. L., Hogan, C. J., Jha, S., Kirshner, R. P., Leibundgut, B., Phillips, M. M., Reiss, D., Schmidt, B. P., Schommer, R. A., Smith, R. C., Spyromilio, J., Stubbs, C., Suntzeff, N. B., and Tonry, J. (1998). Observational Evidence from Supernovae for an Accelerating Universe and a Cosmological Constant. *AJ*, 116:1009–1038.

Riess, A. G., Macri, L., Casertano, S., Sosey, M., Lampeitl, H., Ferguson, H. C., Filippenko, A. V., Jha, S. W., Li, W., Chornock, R., and Sarkar, D. (2009). A Redetermination of the Hubble Constant with the Hubble Space Telescope from a Differential Distance Ladder. *ApJ*, 699:539–563.

Ryden, B. (2003). *Introduction to cosmology*.

Sahni, V., Sathyaprakah, B. S., and Shandarin, S. F. (1994). The evolution of voids in the adhesion approximation. *ApJ*, 431:20–40.

Sathyaprakash, B. S., Sahni, V., Munshi, D., Pogosyan, D., and Melott, A. L. (1995). Gravitational instability in the strongly non-linear regime: a study of various approximations. *MNRAS*, 275:463–482.

Schaap, W. E. and van de Weygaert, R. (2000). Continuous fields and discrete samples: reconstruction through Delaunay tessellations. *A&A*, 363:L29–L32.

SDSS-III collaboration (2011). The Eighth Data Release of the Sloan Digital Sky Survey: First Data from SDSS-III. *ApJS*, 193:29–+.

Sirko, E. and Spergel, D. N. (2005). Reconstruction of the linear power spectrum. In *American Astronomical Society Meeting Abstracts*, volume 37.

Springel, V., White, S. D. M., Tormen, G., and Kauffmann, G. (2001). Populating a cluster of galaxies - I. Results at $z = 0$. *MNRAS*, 328:726–750.

van de Weygaert, R., Kreckel, K., Platen, E., Beygu, B., van Gorkom, J. H., van der Hulst, J. M., Aragon-Calvo, M. A., Peebles, P. J. E., Jarrett, T., Rhee, G., Kovac, K., and Yip, C. . (2011). The Void Galaxy Survey. *ArXiv e-prints*, 1101.4187.

van de Weygaert, R. and Platen, E. (2009). Cosmic Voids: structure, dynamics and galaxies. *ArXiv e-prints*, 0912.2997.

Vikhlinin, A., Kravtsov, A. V., Burenin, R. A., Ebeling, H., Forman, W. R., Hornstrup, A., Jones, C., Murray, S. S., Nagai, D., Quintana, H., and Voevodkin, A. (2009). Chandra Cluster Cosmology Project III: Cosmological Parameter Constraints. *ApJ*, 692:1060–1074.

Walker, A. G. (1937). On Milnes theory of world-structure. *Proc. London Math. Soc.*, s2-42:90–127.

Zel'Dovich, Y. B. (1970). Gravitational instability: An approximate theory for large density perturbations. *A&A*, 5:84–89.

Zwicky, F. (1937). On the Masses of Nebulae and of Clusters of Nebulae. *ApJ*, 86:217–+.